Three-Dimensional Nearshore Currents and Eddies on an Alongshore-Variable Barred Beach

Christine Marie Baker

A thesis
submitted in partial fulfillment of the
requirements for the degree of

Master of Science

University of Washington

2019

Committee:

Nirnimesh Kumar, Chair

Melissa Moulton, Chair

Jim Thomson

Program Authorized to Offer Degree:
Civil and Environmental Engineering

University of Washington

Abstract

Three-Dimensional Nearshore Currents and Eddies on an Alongshore-Variable Barred
Beach

Christine Marie Baker

Co-Chairs of the Supervisory Committee:
Assistant Professor Nirnimesh Kumar
Department of Civil & Environmental Engineering

Senior Research Scientist/Engineer Melissa Moulton
Applied Physics Laboratory

Three-dimensional circulation in the nearshore region is critical for contaminants, sediment, and larvae dispersion along the coast and transport between the surf zone and the inner shelf. In the surf zone, eddies generated by short-crested wave breaking, wave-group forcing, and shear instabilities are associated with energetic vortical motion at very low frequencies ($f \approx 0.005$ Hz), but the horizontal length scales and vertical structure of these vortical motions are poorly understood. Here, a three-dimensional phase-resolving numerical model, Simulating WAves till SHore (SWASH), simulates wave propagation and three-dimensional circulation patterns on a barred beach near Duck, North Carolina. Modeled wave statistics and nearshore currents are consistent with field measurements collected in Oct. 2015. The model accurately simulates the cross-shore wave height gradient, mean alongshore currents, and offshore-directed meanders within the surf zone for a range of offshore wave conditions. Simulated eddy length scales, quantified using the alongshore wavenumber spectra of vorticity, suggest that large-scale eddies ($\mathcal{O}(100)$ m) occur for both alongshore-variable (observed) and alongshore-uniform (alongshore mean of observed) bathymetry, and may be enhanced by surfzone bathymetric variability. Small-scale eddies ($\mathcal{O}(10)$ m) generated by short-crested breaking and wave-group forcing have similar eddy variance for simulations

with alongshore-uniform and alongshore-variable bathymetry. The depth dependence of the alongshore wavenumber spectra of vorticity magnitude and peak length scales varies with cross-shore location and bathymetric variability. The complex vertical structure of the energy, coherence, and phase of very low-frequency vortical motion for both alongshore-variable and alongshore-uniform bathymetry may be associated with the vertical structure of eddy injection, instabilities, mean shear, and bottom boundary layer dynamics.

TABLE OF CONTENTS

LIST OF FIGURES

LIST OF TABLES

ACKNOWLEDGMENTS

Chapter 1

INTRODUCTION

The nearshore is a transition region from the land to the ocean that extends several kilometers offshore and consists of the surf zone (from the shoreline to the seaward extent of depth-limited wave breaking) and the inner shelf (seaward from the surfzone edge to about 1.5 km offshore). Understanding circulation dynamics and tracer dispersion in the nearshore is critical given the concentration of recreational, commercial and ecosystem resources in this region [*Boehm et al.*, 2017]. Species inhabiting the nearshore (*e.g.,* intertidal invertebrate gametes) exploit cross-shore circulation for recruitment and settlement [*Pineda et al.*, 2007; *Shanks et al.*, 2010]. Pollutants and pathogens causing gastrointensial infections and requiring beach closures may be diluted or concentrated by nearshore currents [*Stoner and Dorfman*, 2007]. In addition, excess nutrient supply from terrestrial runoff may lead to eutrophication in coastal zones, creating hypoxic conditions that threaten benthic organisms and ecosystem health.

The surf zone and the inner shelf are dynamically distinct regions. Inner-shelf circulation is driven primarily by cross- and alongshore winds, barotropic and baroclinic tides, and submesoscale dynamics. In contrast, surfzone circulation is driven by complex interactions between surface waves, bathymetric irregularities, and bottom boundary layer dynamics. Mean cross-shore flows in the surf zone are characterized by a balance between radiation stress gradients, barotropic pressure gradients, and a weaker contribution from bottom stress, resulting in wave setup and an offshore return flow [*i.e.,* 'undertow', *Longuet-Higgins and Stewart*, 1964; *Bowen et al.*, 1968; *Stive and Wind*, 1982; *Raubenheimer et al.*, 2001]. Wave-induced alongshore currents result from cross-shore gradients of the off-diagonal component of the radiation stress tensor [*Longuet-Higgins*, 1970; *Feddersen et al.*, 1998; *Garcez-Faria*

et al., 1998], primarily balanced by the bottom stress [*Visser*, 1986; *Simons et al.*, 1992; *Reniers et al.*, 2004b].

The vertical structure of both cross- and alongshore velocities depends on the vertical distribution of the momentum flux generated by surface-wave breaking, bottom friction, and the interaction with three-dimensional circulation induced by bathymetric irregularities [*Putrevu et al.*, 1995; *MacMahan et al.*, 2004a]. Wave breaking over alongshore bathymetric variations drives bathymetric rip currents and meandering alongshore currents including cell-like circulation patterns [*MacMahan et al.*, 2006; *Dalrymple et al.*, 2011]. The mean circulation (timescales of hours) varies with changes in the wave forcing [*Reniers et al.*, 2004a; *MacMahan et al.*, 2004b] and the tidal elevation [*Thornton and Kim*, 1993] over spatial scales over which wave conditions and bathymetry vary [*Long and ÖzkanHaller*, 2005]. Multiple field and numerical modeling studies have investigated the vertical structure of mean flows, including the parabolic vertical profile of undertow [*Garcez-Faria et al.*, 1998] and the logarithmic vertical structure of mean alongshore currents [*Garcez-Faria et al.*, 2000; *Reniers et al.*, 2004b]. However, only a few field and numerical modeling studies investigate the three-dimensional structure of complex nearshore currents in a field environment with alongshore-varying bathymetry, and little is known about the vertical structure of flows at timescales shorter than the mean circulation.

1.0.1 Surfzone vortical motion

Low-frequency eddy activity contributes to dispersion and mixing, thus affecting the transport of traces along the coast as well as between the surf zone and the inner shelf [*Spydell and Feddersen*, 2009; *Clark et al.*, 2010, 2011; *Suanda and Feddersen*, 2015]. Low-frequency infragravity motion ($0.004 < f < 0.04$ Hz) is linked to wave groups [*Guza and Thornton*, 1985; *Elgar and Guza*, 1985] and alongshore propagating edge waves generated by free-surface gravity waves [*Eckart*, 1951; *Bowen and Guza*, 1978]. Vortical motions with periods of 200 s and greater ($f \approx 0.005$ Hz), referred to as very low-frequency (VLF) motion, may be generated by shear instabilities [*Bowen and Holman*, 1989; *Oltman-Shay et al.*, 1989;

ÖzkanHaller and Li, 2003], wave-group forcing [Haller et al., 1999; Long and Özkan Haller, 2009], and finite-crested wave breaking [Peregrine, 1998; Johnson and Pattiaratchi, 2006; Bonneton et al., 2010].

Field measurements from the SUPERDUCK experiment revealed eddy activity at frequencies of 0.002–0.02 Hz, with length scales of 40–250 m, which was attributed to shear instabilities in mean alongshore current driven by obliquely incident waves [Oltman-Shay et al., 1989]. Shear-instability generated eddies have also been studied with numerical modeling [Longuet-Higgins, 1973; Allen et al., 1996; Peregrine, 1999] and theoretical framework [Bowen and Holman, 1989; Dodd et al., 1992; Feddersen, 1998].

Wave-group driven alongshore radiation stress gradients from alongshore wave-breaking variability may also contribute to surfzone eddy generation with length scales $\mathcal{O}(10-100)$ m [Haller et al., 1999; Reniers et al., 2004a; Long and Özkan Haller, 2009]. Surfzone eddies formed by obliquely incident wave groups are advected by mean alongshore currents with similar frequency-wavenumber characteristics to shear instabilities [Long and Özkan Haller, 2009]. Wave-averaged numerical models with wave-group forcing explain observed surfzone eddy-induced velocities on rip-channeled beaches for near shore-normal wave conditions with near-zero alongshore mean flow [Reniers et al., 2007, 2009; MacMahan et al., 2010].

Injection of vorticity into the surf zone at length scales of $\mathcal{O}(10)$ m by individual finite-crested breaking waves [Peregrine, 1998; Johnson and Pattiaratchi, 2006; Bonneton et al., 2010] has been measured in the field [Clark et al., 2012]. Short-crested wave-breaking generated vorticity is hypothesized to coalesce to larger scales of $\mathcal{O}(100)$ m due to an inverse energy cascade [Kraichnan, 1967; Rutgers, 1998; Boffetta and Ecke, 2012]. Low-frequency surfzone current measurements had a peak in energy at 0.005 Hz, suggestive of a hypothesized inverse cascade [Elgar et al., 2019]. Eddy-injection and evolution in strongly sheared alongshore currents also have similar frequency-wavenumber characteristics to those due to shear instabilities [Feddersen, 2014]. Cross-shore mixing and tracer dispersion due to short-crested breaking is found to be suppressed in presence of strong alongshore flows [Spydell, 2016].

The vertical structure of VLF vortical motion in the surf zone is not known, in part because field measurements often sample flows at a single elevation, and vortical motions are difficult to estimate given the horizontal spacing of sensor arrays. Two recent field studies in Duck, NC have investigated the depth dependence of low-frequency eddies in the surf zone [*Lippmann et al.*, 2016; *Henderson et al.*, 2017]. A cross-shore array of vertically stacked electromagnetic (EM) current sensors sampling at 8 Hz measured the vertical structure of the cross- and alongshore currents during the Duck94 experiment. The vertical structure of energy, phase, and rotary spectral quantities at VLF frequencies indicate substantial depth variability linked with bottom boundary layer dynamics and shear in alongshore velocities [*Lippmann et al.*, 2016; *Lippmann and Bowen*, 2016].Low-frequency motion measured with Acoustic Doppler Profilers was relatively depth-uniform within the surf zone [*Henderson et al.*, 2017]. Depth dependence in the eddy structure was observed outside of the surf zone, and depth dependence decreased in regions with strong wave breaking in the surf zone [*Henderson et al.*, 2017].

1.0.2 *Nearshore circulation modeling*

Phase-averaged models of nearshore circulation simulate the evolution of the wave energy spectrum (*e.g.,* SWAN) and have been used extensively to study the role of wave-energy dissipation in driving mean flows in the surf zone. These models are skillful at reproducing wave-induced dynamics, including rip-current circulation, alongshore currents, and wave setup [*e.g., Reniers et al.*, 2004b; *Uchiyama et al.*, 2010; *Kumar et al.*, 2012]. However, phase-averaged numerical models do not directly simulate the wave-induced vorticity associated with energy dissipation from short-crested wave breaking, and parameterizations of these processes have not been tested thoroughly.

Phase-resolving models, which simulate individual wave propagation, are often based on vertically integrated, time-dependent mass and momentum balance equations, and can simulate eddies generated by finite-crested wave breaking. Phase-resolving Boussinesq models (*e.g.,* funwave/funwaveC) solve equations similar to the nonlinear shallow-water equations,

while also including higher order dispersive terms [*Okey*, 1993], and have been used to study eddy generation dynamics and the associated cross-shore exchange [*Feddersen*, 2014; *HallyRosendahl and Feddersen*, 2016]. However, these models do not account for stratification effects or resolve vertical variability of horizontal velocities, which are important for cross-shelf exchange. Furthermore, length scales associated with vortical VLF motions have been explored for depth-integrated flows in alongshore-uniform beaches [*e.g., Feddersen et al.*, 2011; *Feddersen*, 2014; *Kumar and Feddersen*, 2017], but have not been explored for depth-varying flows on a beach with complex bathymetry.

Coupled ocean-circulation and phase-averaged models (*e.g.,* COAWST) simulate vertically varying surfzone circulation [*Warner et al.*, 2010; *Kumar et al.*, 2012]. One-way coupling between three-dimensional circulation models with depth-averaged phase-resolving models (*e.g.,* funwaveC) include patterns of bulk vorticity injection similar to that resulting from short-crested wave-breaking [*Kumar and Feddersen*, 2017]. However, this approach may result in aliasing of the rotational wave forcing due to the smaller time steps in the phase-resolving simulations, and does not include two-way coupled wave-current interactions between three-dimensional eddies and propagating waves. Additionally, non-hydrostatic pressure perturbations, which may be important for eddy interaction with stratification, are not included in hydrostatic phase-averaged modeling approaches.

A three-dimensional phase-resolving model, such as Simulating WAves til SHore (SWASH) or NHWAVE, includes the physics needed to study three-dimensional VLF motion forced by dynamics such as short-crested wave breaking. SWASH, a three-dimensional phase-resolving non-hydrostatic numerical model developed to study transformation of dispersive surface waves from offshore to the beach, simulates wave-forced eddy generation and three-dimensional circulation [*Zijlema et al.*, 2011]. SWASH solves nonlinear shallow water equations including non-hydrostatic pressure to allow for conservative transport of temperature, salinity, and suspended sediment [*Zijlema and Stelling*, 2005]. The second-order accuracy allows for more computationally efficient simulations than Boussinesq models, while correcting for frequency dispersion through the addition of more vertical layers [*Zijlema et al.*,

2011]. SWASH has been used extensively to study nearshore wave breaking [*Smit et al.*, 2013], infragravity wave dynamics [*Rijnsdorp et al.*, 2012, 2014], nonlinear infragravity-wave interactions [*de Bakker et al.*, 2016], run-up oscillations [*Ruju et al.*, 2014] and nonlinear wave-dynamics [*Smit et al.*, 2014]. However, the ability of SWASH to accurately simulate three-dimensional surfzone circulation had not been tested previously.

In this paper, SWASH is used to simulate three-dimensional wave propagation and circulation on a beach with complex alongshore-varying bathymetry. The model is compared with observed hour-average wave statistics and circulation from Duck, North Carolina for three time periods spanning a range of wave conditions. The alongshore length scales and vertical structure of vortical motion in the surf zone are quantified for a simulation with observed bathymetry and contrasted against those for simulations with less alongshore bathymetric variability.

Chapter 2

METHODS

2.1   Field Experiment

2.1.1   Experiment Overview

Field observations were collected on an alongshore-inhomogeneous barred beach near Duck, North Carolina at the United States Army Corps of Engineers Field Research Facility (FRF, http://frf.usace.army.mil/frf.shtml) as part of the BathyDuck2015 Experiment, a large effort to evaluate and improve coastal numerical models [*Smith et al.*, 2017]. Measurements from this experiment include offshore wave sensors at water depths of 11 m ($x = 1295$ m, $y = 978$ m) and 6 m ($x = 606$ m, $y = 937$ m) and an array of collocated pressure sensors and acoustic current meters in the surf zone, sampling at 2 Hz (Figure 2.1). The coordinate system used here is the FRF coordinate system, in which the cross-shore coordinate, x is positive offshore, the alongshore coordinate, y is positive to the north, the vertical component, z is positive upward and referenced to the NAVD88 datum (approximately local mean sea level), and time is reported in local time (EDT). Two cross-shore transects of four collocated ADVs and pressure sensors were deployed from $z = 1.5$–3.5 m, separated by 125 m in the cross-shore and 75 m in the alongshore (Figure 2.1). In addition, two sensors were deployed south of these arrays close to the FRF pier. The nearshore sensors were positioned 0.5 to 1 m above the bed.

2.1.2   Bathymetry

Bathymetry data was collected on October 14, 2015 with the Lighter Amphibious Resupply Cargo (LARC) vehicle using a single-beam acoustic sonar and RTK GPS. The bathymetry

measurements spanned 0.9 km cross-shore ($x = 50$–950 m) to a depth of 9 m and 1 km alongshore ($y = $ -100–1100 m) (Figure 2.1). On October 14, the average shoreline position was approximately $x = 108$ m, and the beach had a bar near $x = 225$ m with an alongshore-variable trough near $x = 150$ m. A scoured channel was located under the pier at $y = 500$ m. Sub-regions of the domain ($x = 62$–626 m, $y = 548$–980 m) surveyed with the Coastal Research Amphibious Buggy (CRAB) on October 19 and 30, 2015 show that the large-scale patterns with bar-trough ($y = 650$–800 m) and plateau ($y = 800$–850 m) regions persisted through the end of October (not shown here). Bathymetry data collected with the LARC for the entire region on November 16, 2015 shows less alongshore variability nearshore (*e.g., y* $= $ -100–500 m) than measured during the previous survey, a 10 m shoreward shift of the bar crest (from $y = 600$–1100 m), and a southward shift of bathymetric features (*e.g.,* trough y $= 650$–800 m, not shown here).

2.1.3   Wave Conditions

ADV measurements were quality controlled [*Elgar et al.*, 2005] and used to compute nearshore hourly bulk wave parameters (*e.g.,* significant wave height, mean currents, wave direction, and directional spread), reported as the average of six 512-second data collections over each hour. A frequency-dependent correction for depth using linear wave theory was applied to nearshore pressure measurements to estimate sea-surface elevation statistics [*Guza and Thornton*, 1980]. The wave conditions measured by an offshore wave sensor at 11 m water depth and a nearshore sensor at 2 m water depth are shown in Figure 2.2. The tidal elevation (η) measured by a NOAA tide gauge in 6 m depth ($x = 582$ m, $y = 509$ m) varied from 1 to 1.6 m (Figure 2.2a). Significant wave heights (H) were computed by integrating the energy spectral density over frequency bands from 0.05 to 0.30 Hz. The energy-weighted wave angles (θ) and directional spread (σ_θ) were computed for the same frequency range using directional moments. Incident waves from counter-clockwise (from the north-east) and clockwise (from the south-east) of shore-normal are reported as $\theta > 0°$ and $\theta < 0°$, respectively. The offshore significant wave height ranged from 0.3 to 2.0 m during the experiment (Figure 2.2b). The

wave incidence angles at the offshore wave buoy varied from -45° to 50° (black, Figure 2.2c). The offshore wave directional spread was between 25° to 40° (black, Figure 2.2d) and the offshore peak wave periods ranged from 4 to 12 s (not shown). The maximum hourly-average nearshore current speeds were approximately 0.8 m/s. Two large wave events occurred during the experiment with significant wave heights of 1 to 2 m. During the first large wave event on October 18 to 20, the waves were predominantly from the north-east ($\theta > 0°$) whereas during the second large wave event on October 26 to 30, the mean wave direction was within 15 degrees of the shore-normal for the majority of the wave event. The wave energy spectrum was bi-modal from October 14 10:00 to October 17 23:00 EDT with peak frequencies near 0.13 and 0.25 Hz.

2.2 Numerical Modeling

2.2.1 Model Description

Nearshore circulation and wave propagation was simulated using Simulating WAves till SHore (SWASH), an open source non-hydrostatic wave-flow model [*Zijlema et al.*, 2011]. This three-dimensional model solves the nonlinear shallow water equations including horizontal momentum equations with non-hydrostatic pressure and a vertical momentum equation [*Zijlema and Stelling*, 2005]. SWASH, based on an explicit, second-order finite difference method for horizontally staggered grids, conserves mass and momentum at discrete levels for incompressible fluid with a constant density, which enables an efficient scheme to simulate individual wave propagation and breaking with high spatio-temporal resolution. The momentum equations are

$$\frac{\partial u_i}{\partial t} + \frac{\partial u_i u_j}{\partial x_j} = -\frac{1}{\rho}\frac{\partial(p_h + p_{nh})}{\partial x_i} - g + \frac{\partial \tau_{ij}}{\partial x_j} \tag{2.1}$$

and

$$\frac{\partial u_j}{\partial x_j} = 0 \tag{2.2}$$

where u_i and u_j are horizontal and vertical velocity components. Here, t is time, ρ is density, g is gravitational acceleration, p_h and p_{nh} are hydrostatic and non-hydrostatic pressure

components, and τ_{ij} are turbulent stresses. The time evolution of the surface elevation is determined by continuity,

$$\frac{\partial \eta}{\partial t} + \frac{\partial}{\partial x_j} \int_{-h}^{\eta} u_j dz = 0 \tag{2.3}$$

where h is the stationary bottom boundary and η is the moving free-surface.

The vertical turbulent mixing of momentum and material (*e.g.,* salt, heat and suspended sediment) is parameterized through a two-equation turbulence closure model ($k - \epsilon$). The bottom friction is provided as a shear stress term. The vertical eddy viscosity allows for diffusion of this stress into the water column including coupling between vertical layers, and also increases numerical stability [*Smit et al.*, 2013]. The surface and bottom kinematic boundary layers constrain particle motion, providing the constraints at the fixed bottom,

$$u_j = -u_i \frac{\partial \eta}{\partial x_i} \tag{2.4}$$

and the free-surface,

$$u_j = \frac{\partial \eta}{\partial t} + u_i \frac{\partial \eta}{\partial x_i} \tag{2.5}$$

where there is a constant pressure ($p_h = p_{nh} = 0$) and no surface stresses at the free-surface. The bottom boundary shear stress, τ_b is based on a quadratic friction law, with the drag coefficient, c_f determined from the Manning-Strickler formulation such that

$$c_f = 0.015(k/h)^{1/3} \tag{2.6}$$

where k is the apparent roughness [*Smit et al.*, 2013].

SWASH simulates wave breaking using a hydrostatic front approximation, similar to disabling dispersive terms in the Boussinesq equations [*Tissier et al.*, 2012; *Tonelli and Petti*, 2010], and by prescribing a hydrostatic pressure distribution in the model around the discontinuity of a breaking wave. The turbulent wave-front is regarded as a sub-grid flow feature where the vertical accelerations are not resolved and the non-hydrostatic pressure is set to zero. The hydrostatic front approximation is initiated when local surface steepness exceeds a fraction of the shallow water celerity,

$$\frac{\partial \eta}{\partial x} > \alpha \sqrt{g(h + \eta)} \tag{2.7}$$

where α is a parameterized value. The spatial persistence of wave breaking is achieved by labeling a mesh-point for hydrostatic computation if the neighboring grid point has been labelled for hydrostatic computation and the local steepness exceeds a fraction of the shallow water celerity (Equation 2.7) where the parameterized value is replaced with β. This approach, combined with the conservation of momentum, leads to appropriate levels of energy dissipation on the front face of a breaking wave [*e.g., Peregrine*, 1983].

2.2.2 Model Testing Setup

In this study, SWASH is run on a 2-m-resolution horizontal grid spanning 1.5 km alongshore and 0.9 km cross-shore from the shoreline to 9 m water depth. Simulations were run with 5 vertical layers, resolving depth-varying flows while maintaining simulation efficiency and stability. All simulations were conducted for 2 hours with an initial time step of 0.04 seconds and a cycle length (repeated length of the time series realization) of 1 hr. The first hour is allotted for model spin up, and 1 Hz output for the second hour is used for analysis. SWASH simulation results are presented in the FRF coordinate system.

The simulation stability was improved by discretization with flux-limited (shock-resolving) vertical advective terms indicated with the first-order upwind scheme. The MUSCL limiter is introduced for water depth in velocity points and for the horizontal advective terms in the horizontal and vertical momentum equations. A 10^{-3} m^2/s background eddy viscosity was introduced to simulations to account for unresolved vertical mixing enhancing stability in the model, specifically in the swash zone. This value is small compared with the vertical viscosity computed by the standard $k - \epsilon$ model. Wave breaking is controlled with a threshold parameter for initiation of wave breaking at a mesh-point, $\alpha = 0.6$ [*Lynett Patrick J.*, 2006] and for the neighboring mesh-points, $\beta = 1.0$. Non-hydrostatic pressure gradients in the vertical momentum equations are approximated with the Keller-box scheme [*e.g., Lam and Simpson*, 1976]. Explicit time integration is performed using a specified Courant number between 0.05 and 0.3, and the vertical time integration uses the implicit Euler Scheme. A logarithmic roughness with a 1-mm roughness length was applied for bottom friction.

Simulations were run with the observed bathymetry from the survey closest to the date of the simulations (October 14) interpolated to the model grid with the hour-averaged tidal elevation applied. Periodic boundary conditions were used on the north/south domain boundaries. The domain was extended alongshore on the northern and southern boundary by 124 m, converging exponentially to an alongshore averaged bathymetry to allow for periodic boundary conditions. The model was forced at the offshore boundary with H, T_p, θ, and σ_θ measured at 11 m water depth. The model generates a JONSWAP spectrum from these bulk wave inputs. The peakedness parameter, γ_J for a JONSWAP spectrum was calibrated to match the observed spectra. Several model simulations were conducted for wave conditions representative of the range of hourly observed conditions to test SWASH's ability to simulate processes in and near the surf zone for a variety of conditions.

2.3   Very Low-Frequency Flow Analysis

Frequency and rotational statics are computed with 1 Hz time series from the second hour of each simulation (3600 - 7200 s) to investigate eddy length scales and depth dependence. SWASH divides the computational domain into a fixed number of vertical time-evolving terrain-following sigma layers. The horizontal velocities at the sigma layers are interpolated to specific elevations between the mean sea-surface elevation and the bed. Near-surface velocities are selected at the fixed vertical grid point that is one half of the alongshore averaged significant wave height below the mean sea-surface elevation. Near-bottom velocities are selected at the vertical grid coordinate closest to 3 cm above the bed, typically outside of a wave bottom boundary layer. Temporal velocity spectral analyses are performed using a Hanning window length of 512 s with an overlap length of 256 s for a 3600 s velocity time series yielding a $\Delta f = 0.002 Hz$ with the lowest bin centered at $f = 0.002$ Hz. The low-pass filter provides the cross- (u) and alongshore (v) velocity at very low-frequencies (VLFs), defined as as $0.003 < f < 0.007$ Hz, which are used to compute the root mean squared (rms) VLF velocities relative to the rms near-surface velocity ($u_{rms}/u_{0,rms}$, $v_{rms}/v_{0,rms}$). The VLF spectral density (S_{uu}, S_{vv}) is computed as the sum of the frequency bins centered

at $f = 0.004$ and 0.006 Hz. The VLF velocity squared coherence (λ_u^2, λ_v^2) and phase relative to the near-surface VLF velocity (ϕ_u, ϕ_v, positive and negative phase indicate leading and lagging surface velocities) is computed as the average over those bins.

The extent to which energy associated with surfzone horizontal motions is explained by sea-surface fluctuations under linear shallow-water surface gravity wave theory is assessed by comparing the sea-surface elevation spectrum ($S_{\eta\eta}$) multiplied by the gravity (g) over the time-average water depth (h) with the sum of the cross- and alongshore velocity spectrum (S_{uu}, S_{vv}) (Figure 2.3). At frequencies where horizontal motions are consistent with surface gravity waves (e.g., swell and infragravity waves), $S_{\eta\eta} * g/h$ is similar in magnitude to $S_{uu} + S_{vv}$. Conversely, at lower frequencies, where surfzone energy may be dominated by vortical motion (e.g., the VLF band) that is not associated with large sea-surface variations, $S_{uu} + S_{vv}$ is much greater than $S_{\eta\eta} * g/h$. Within the VLF band, the velocity variance is 20 to 40 times greater than the variance from surface motions, suggesting that vortical motion is dominant.

In addition to spectra of horizontal velocities and pressure, rotary spectra are computed to isolate the rotational motion associated with surfzone eddies. The rotary spectra are estimated by decomposing the horizontal velocity components into clockwise (CW) and counter-clockwise (CCW) components [*Gonella*, 1972]. The complex velocity is defined as

$$R = u + iv \tag{2.8}$$

When a Fourier decomposition of u and v,

$$u(t) = a_1 \cos(\omega t) + b_1 \sin(\omega t) \tag{2.9}$$

$$v(t) = a_2 \cos(\omega t) + b_2 \sin(\omega t) \tag{2.10}$$

is substituted into the complex velocity (Equation (2.8)), this yields,

$$R = R^+ e^{i|\omega|t} + R^- e^{i|\omega|t} = (R^+ + R^-)\cos(|\omega|t) + (R^- + R^+)i\sin(|\omega|t) \tag{2.11}$$

where R^- is the CW velocity and R^+ is the CCW velocity. By applying trigonometric identities, the components can be further decomposed into

$$R^+ = \frac{1}{2}\left(a_1 + b_2 + i(a_2 - b_1)\right) \tag{2.12}$$

$$R^- = \frac{1}{2}\left(a_1 - b_2 + i(a_2 + b_1)\right) \tag{2.13}$$

The VLF rotational motion spectra (S_{rot}) shown in the results are the sum of the CW and CCW rotational components, indicating the total variance in rotational motions. The squared coherence (λ_{rot}^2) and phase (ϕ_{rot}) relative to the near-surface are shown as the average of the results for the CW and CCW rotational components, indicating average patterns of these quantities. The rotary coefficient (C_R) describes the relative magnitude of CW and CCW rotary components and is computed as:

$$C_R = \frac{S_{cw} - S_{ccw}}{S_{cw} + S_{ccw}} \tag{2.14}$$

where $-1 < C_R < 1$ indicating CW ($C_R > 0$) and CCW ($C_R < 0$) rotation.
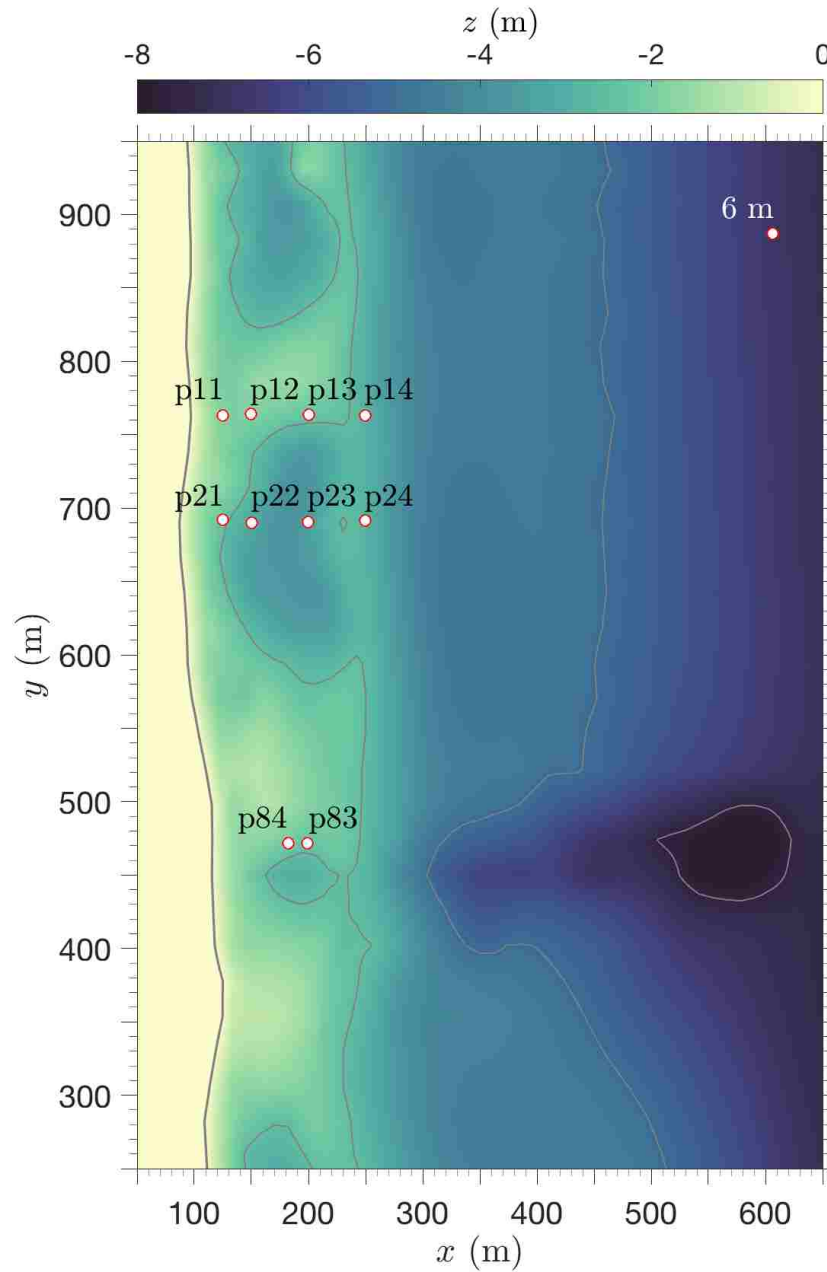
Figure 2.1: Locations of ADVs and pressure gauges (red symbols) and bathymetry measured on October 14, 2015 (z, color contours) versus cross-shore (x) and alongshore coordinates (y). The alongshore-varying sandbar-trough and terrace system is interrupted by channels. The deep channel at around $y = 500$ m is formed from scour near the FRF pier.
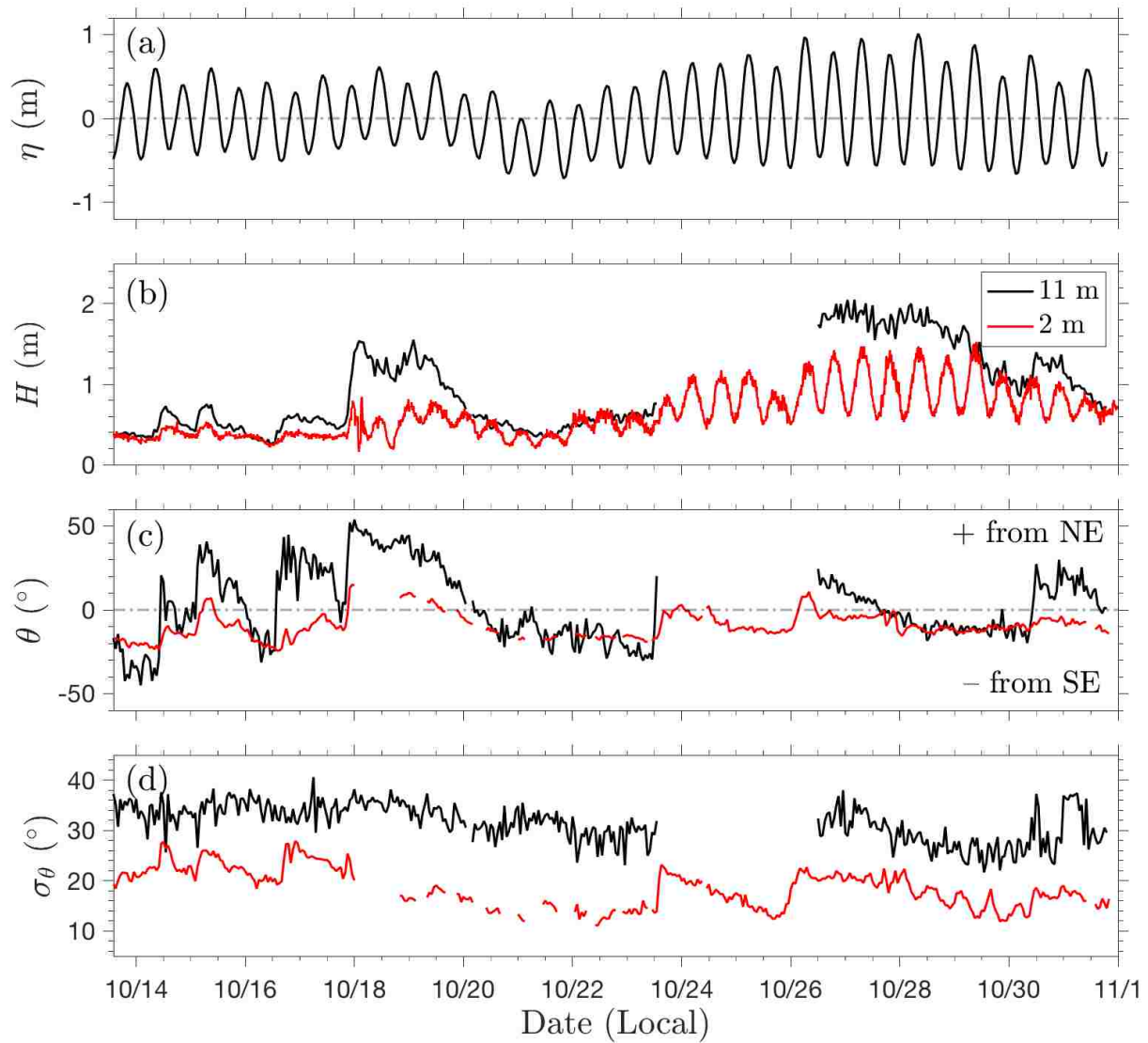
Figure 2.2: Hour-average (a) tidal elevation, η, measured in 6 m depth and (b) wave height, H, (c) direction, θ, and (d) directional spread, σ_θ, measured in 11 m depth (black) and approximately 2 m depth (p22 at $x = 150$ m and $y = 740$ m) (red).
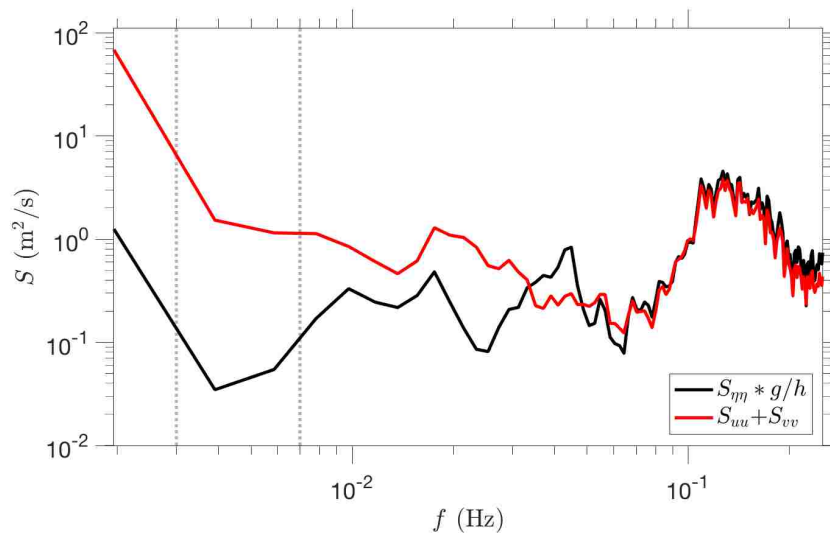
Figure 2.3: The relative variance of the sea-surface elevation spectra times the gravity (g) over time-averaged water depth (h) (black) and the sum of the cross- and alongshore spectra (S_{uu}, S_{vv}) (red) in the surf zone at $(x, y, z = 132,740,-1.8)$ m. Vortical motion is the dominate energy source in the VLF band (dashed lines).

Chapter 3

RESULTS

3.1 Numerical Modeling Trials

The data collected for a wide range of wave conditions (Figure 2.2) is used to assess the capability of SWASH to simulate nearshore circulation over complex bathymetry. Here, the model-observation comparison results are discussed for three simulations with forcing representative of the range of observed conditions, including directionally spread small and large waves with a large directional spread with a mean direction that is normally incident or oblique to the beach (Table 3.1). Simulation S1 and S2 were selected to compare oblique and shore-normal directionally spread low-energy wave conditions. Simulation S3 has normally incident high-energy wave conditions, which drive strong surfzone currents. The outer edge of the surf zone (x_{sz}) is defined here as the cross-shore location with the maximum cross-shore gradient in the alongshore-averaged significant wave height, $d\langle H\rangle_y/dx$ (Figure 3.3, white dashed).

The numerical framework and stability of SWASH impacted the selection of the test cases. For conditions with highly oblique directionally spread waves ($> 30°$), alongshore banding of the significant wave height resulted from interference of the limited directional components that could be included in the domain geometry, and thus, these highly oblique conditions are not represented in this analysis. In addition, SWASH became unstable in the swash zone for large oblique waves conditions not shown here. Simulations were forced with a JONSWAP spectrum generated by bulk wave parameters, and therefore, time periods with bi-modal wave spectra, including early in the experiment from Oct. 14 to 18, 2015 were not chosen for SWASH simulations. Differences in the spatial patterns of modeled and observed nearshore waves and currents are expected as the surfzone bathymetry evolved through the

experiment while constant bathymetry measured on October 14 is used all of the simulations.

Table 3.1: Simulated observed conditions at three times during the experiment with an hour-average tidal elevation (η) and offshore (11-m depth) significant wave height (H), peak wave period (T_p), incident wave angle ($\theta = 0°$ is shore-normal, $\theta < 0°$ indicates waves from the southeast), directional spread (σ_θ), and the JONSWAP gamma value (γ_J). The cross-shore location of the seaward edge of the surf zone is x_{sz}.

Sim. No.	Date	Time (EDT)	η (m)	H (m)	T_p (sec)	θ (°)	σ_θ (°)	γ_J	x_{sz} (m)
S1	Oct. 20	10:00	-0.03	0.62	7.8	-3.4	30.8	1.9	180
S2	Oct. 20	15:00	0.13	0.51	8.8	-15.0	29.5	1.8	158
S3	Oct. 28	00:00	-0.32	1.95	8.0	-2.1	28.6	1.4	260

3.2 Comparison of Observed and Modeled Nearshore Conditions

3.2.1 Wave Spectra

Modeled wave spectra are compared with observed spectra at the offshore boundary and in 6 m depth (Figure 3.1). The model is forced at the offshore boundary by a JONSWAP spectrum generated by the model based on the bulk spectral input parameters for conditions observed in 11 m depth (Table 3.1). The generated JONSWAP spectra applied as a boundary condition are similar to the observed spectra (Figure 3.1, black curves). The modeled and observed spectra in 6 m depth also are similar, with similar peak frequencies and spectral distributions (Figure 3.1, red curves). However, differences between the observed and modeled spectra at 6 m depth may result from a combination of differences in the offshore spectrum (Figure 3.1, black curves), inaccurate representation of the spatial variability in the model bathymetry, or uncertainties in the observed spectra.
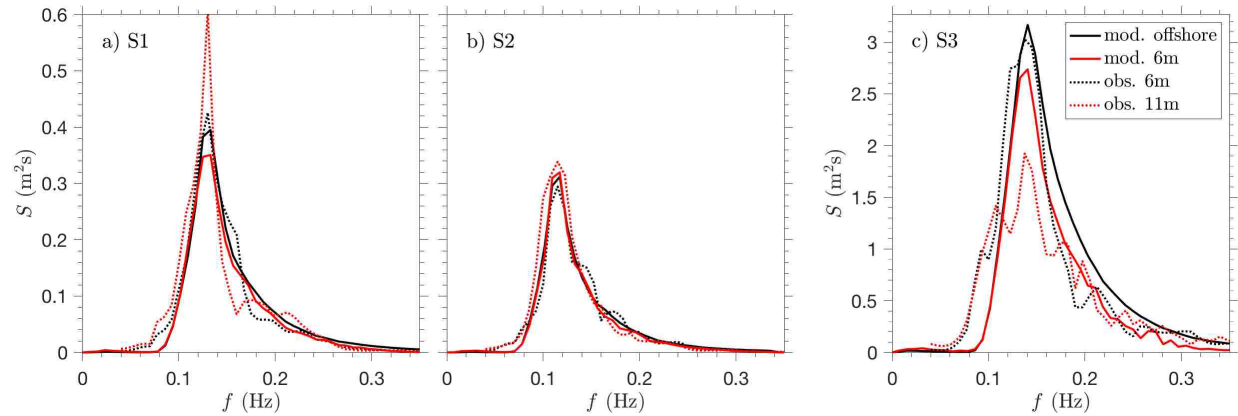
Figure 3.1: Hour-averaged spectra from modeled simulations (solid lines) and observations (dashed lines) at offshore (black curves, model is alongshore-averaged on the offshore boundary, observation is 11 m depth) and 6 m depth (red curves, Figure 2.1) locations for simulations S1 (a), S2 (b), and S3 (c).

3.2.2 Bulk Wave and Velocity Statistics

The observed and modeled significant wave height, cross- and alongshore velocity, mean wave direction, and directional spread are compared (Figure 3.2). Significant wave heights are correlated ($R^2 = 0.54$), however the model over-estimates the wave height (bias = 0.28 m), especially for large-wave conditions (S3, Figure 3.2a, blue dots). The wave breaking parameters, α and β were set to standard values from the literature and were not tuned to this dataset. The average velocities at model grid points closest to the sensor locations have a small average bias (bias = 0.06 m/s), however the correlation is somewhat weak ($R^2 = 0.24$) and at some locations the model velocities are much larger than the observed velocities, particularly for the large-wave simulation (S3, Figure 3.2b, blue symbols). The modeled simulates the observed sign of the mean wave angle in the surf zone (Figure 3.2c). However, there is a large bias ($R^2 = 0.37$, bias = 8.1°), which may result from errors in the model bathymetry or compass errors in the observed wave forcing. The magnitude of the simulated and observed directional spreads are similar (Figure 3.2d). The use of a constant model

bathymetry measured one to two weeks prior to the simulated time periods is likely a large source of the model data disagreement due to the sensitivity of wave direction, spreading, and breaking patterns to local bathymetric irregularities in the surf zone.

3.2.3   Three-dimensional flow patterns

Modeled and observed wave breaking patterns (Figure 3.3d-f) and resulting breaking-wave driven currents (Figure 3.3a-c) are compared, and the vertical structure of modeled mean flows is investigated (Figure 3.4). The simulations and observations show similar patterns of wave heights, with decreasing heights with wave breaking on the surfzone bathymetry (Figure 3.3d-f), and wave refraction occurs near the pier ($y = 500$ m) and over the complex surfzone bathymetry. The observed and simulated flows include alongshore flows that are strongest near the shoreline and meander around prominent bathymetric features, along with strong offshore-directed flows resulting from bathymetric rip-current circulation (Figure 3.3a-b). S1 and S2 reproduce the observed alongshore flow and offshore-directed meanders near channels and other bathymetric features, as well as weak flows in the center of the circulation cell ($y = 740$ m). The simulated flows in S2 are stronger than the observed flows for the sensors at the outer edge of the surf zone ($x = 250$ m). For S3, the modeled circulation is shifted in the positive alongshore direction relative to the observations, possibly due to migration of bathymetric features resulting from longshore currents present from Oct 18th to 20th.

Cross-shore transects of the hour-average horizontal velocity and vorticity indicate complex vertical structure in the flow field (*e.g.,* Figure 3.4). For the simulated and observed velocities of the case with large wave conditions (S3, Table 3.1), this cross-shore transect ($y = 740$ m, near stations p21-24) intersects the center of a 200-m wide circulation cell, with strong average alongshore velocities in the inner surf zone that weaken and change sign in the trough (Figure 3.3c). The modeled Eulerian mean cross-shore velocity is primarily offshore, likely a combination of an offshore-directed current as part of a circulation cell and a near-bed return flow (undertow) balancing Stokes drift (Figure 3.4a). On the shoreward side of the bar crest, the cross-shore velocity changes from onshore near the surface to strongly

offshore near the bottom, which may result from the vertical distributions of wave forcing and pressure gradients. The modeled alongshore average velocities do not change sign in the vertical, but do vary in magnitude in the vertical within the surf zone, where the strongest flows are in the inner surf zone ($100 < x < 150$ m, Figure 3.4b) as part of a meandering along-shore flow (Figure 3.3c). The modeled velocities have similar sign and spatial variations to the measured near-bed velocities (Figure 3.4a,b, symbols). Discrepancies between the modeled and observed velocity may be resulting from differences in the model bathymetry and the actual bathymetry (not measured) at the time corresponding to the wave conditions in the simulation.

The magnitude of the mean vertical vorticity varies with depth, and the sign fluctuates from negative on the on-shore side of the trough to positive on the on-shore side of the bar (Figure 3.4c). The variable vertical and cross-shore structure of the mean flow is an example of complex three-dimensional mean circulation that occurs near nonuniform bathymetry in the surf zone.

3.3 Eddy Length Scales

The length scales of horizontal eddies and their temporal fluctuations are not well understood in alongshore-variable surf zones. Here, the alongshore length scales of surfzone eddies are quantified by averaging 1 Hz estimates of alongshore wavenumber spectra of vertical vorticity ($S_{\omega\omega}$ with spatial mean removed) at each cross-shore grid location ($\Delta x = 2$ m) over the second hour of a simulation. The vertical vorticity for the depth-average and at vertical layers is estimated from gridded velocity components using a central-difference approach [*Patankar*, 1980]. The estimates are computed for alongshore eddy length scales ≥ 10 m ($k/2\pi \geq 10^{-1} m^{-1}$) and for cross-shore positions offshore of the region where swash-zone dynamics are expected to be dominant (mean depths < 0.5 m). The cross-shore coordinate is normalized by the surfzone width L_{sz}, where $x/L_{sz} = 0$ is the mean shoreline position (where the alongshore-averaged seafloor elevation is equal to the mean sea-surface elevation) and $x/L_{sz} = 1$ is the outer edge of the surf zone at position x_{sz}.

3.3.1 Spatial Variability of Alongshore Wavenumber Spectra of Vorticity

The cross-shore variability of depth-averaged alongshore eddy length scales is quantified for energetic oblique wave conditions (S3) over the highly alongshore variable observed bathymetry (measured Oct. 14) (Figure 3.5a). The observed bathymetry has a maximum standard deviation of the alongshore bathymetry in the surf zone ($\sigma_{y,sz}$) of 1.07 m. In the inner to outer surf zone ($0 < x/L_{sz} < 0.75$), the morphology includes bar-trough patterns (*e.g.*, $y = 650$–800 m) and variable terraces (*e.g.*, $y = 550$–650, 800–875 m, Figure 2.1). To contrast the eddy length scales associated with the incident wave field (e.g., short-crested wave breaking) and those associated with the bathymetric variability, $S_{\omega\omega}$ is computed for two additional SWASH simulations, one using bathymetry with half of the variability of the observed bathymetry (S4, $\sigma_{y,sz} = 0.54$ m, Figure 3.5a, arrow), and another using alongshore-averaged observed bathymetry (S5, $\sigma_{y,sz} = 0$ m, solid black, Figure 3.5a) and otherwise the same forcing as in S3 (see Table 3.1).

The total variance of $S_{\omega\omega}$ for S3, S4, and S5 is computed at each cross-shore location for all length scales, and for small (L<100 m) and large (L<100 m) length scales (Figure 3.5b-d). The total variance of all length scales is largest in the surf zone, and drops by an order of magnitude outside of the surf zone (Figure 3.5b). The total variance of small alongshore length-scale eddies ($L < 100$ m) is similar for all simulations, and therefore relatively independent of alongshore bathymetric variability (Figure 3.5c). In the outer surf zone where wave breaking is strong, the variance of small length-scale eddies is much greater than that of large length-scale eddies (Figure 3.5 compare c,d). In the simulations with less alongshore variability, there is a narrower (cross-shore) peak in small length-scale eddy variance, whereas for the observed bathymetry there is no clear peak, possibly resulting from greater cross-shore spread in the surfzone width. These results suggest that the presence small eddies may be most strongly related to the incident wave field, including eddy generation from short-crested breaking wave vorticity injection, rather than a function of surfzone bathymetric variability.

In contrast to small length-scale eddies, the total variance of eddies with large alongshore length scales ($L > 100$ m) increases with increasing bathymetric variability, where the largest spread between the simulations occuring in the surf zone (Figure 3.5d). The increased variance for the alongshore variable bathymetry may be the result of fluctuations in mean circulation cells or enhanced eddy coalescence in the deep trough regions present in the alongshore variable bathymetry cases. The small increase in variance outside of the surf zone for higher bathymetric variability simulations could be the result of fluctuations in bathymetric circulation patterns that extend outside of the surf zone (e.g., rip current jets) or ejections of surfzone eddies.

The magnitudes of the alongshore wavenumber spectra of vorticity varies as a function of cross-shore position and the bathymetric variability in each simulation (color contours, Figure 3.6a-c). The largest magnitude of vorticity variance occurs for the largest eddies ($L > 160$ m), where $S_{\omega\omega}$ is primarily white (*i.e.*, flat, Figure 3.6d, small wavenumbers), with less variance and a red spectrum (*i.e.*, decreasing with larger wavenumbers, similar roll-off for all simulations) at length scales $L < 80$ m (Figure 3.6, large wavenumbers). At smaller length scales, the magnitude of $S_{\omega\omega}$ is relatively independent of the bathymetric variability, and the magnitude is smallest outside of the surf zone, increases near the outer edge of the surf zone, and decreases in the inner surf zone. This suggests that the energy associated with smaller length scale eddy generation may be related to wave induced eddy generation, which is similar for all simulations.

In contrast, the magnitude of larger eddy length scales ($L > 100$ m, smaller wavenumbers) increases with bathymetric variability (Figure 3.6d, compare solid, dot-dashed, and dashed curves of the same color for $L^{-1} < 10^{-2}$). For all simulations, the largest variance occurs for longer eddy length scales ($L > 160$ m) in the inner surf zone ($0.25 < x/L_{sz} < 0.75$), where deep trough and terrace bathymetric features are present. The variance of large eddies is 1.5 to 2 times less for the alongshore-uniform bathymetry (S5) than the observed bathymetry (S3). Near the shoreline ($0 < x/L_{sz} < 0.2$), the maximum variance of the $S_{\omega\omega}$ occurs at length scales > 100 m where swash zone processes along a variable shoreline may dominate

the vorticity field (Figure 3.6a,b) of the bathymetrically variable simulations (S3, S4).

3.3.2   Depth Variability of Alongshore Wavenumber Spectra of Vorticity

While depth-integrated wave-resolving models can be used to study cross-shore variability of eddy length scales, the vertical variability of these length scales is not known. Here, using the three-dimensional phase-resolving model simulations, the alongshore wavenumber spectra of vorticity at different elevations ($S_{\omega\omega}$, computed with interpolated horizontal velocities, Section 2.3) are used to investigate the vertical variability of eddy length scales. Similar to the depth-averaged analysis, $S_{\omega\omega}$ are computed over the second hour at several cross-shore positions and elevations in the water column (Figure 3.7, S3: top row, S5: bottom row, S4 not shown).

Consistent with the depth-averaged velocity $S_{\omega\omega}$ estimates, the depth-varying $S_{\omega\omega}$ at larger length scales ($L >100$ m) have larger magnitudes for the alongshore-varying (S3) than the alongshore-uniform (S5) bathymetry at all cross-shore locations (compare top to bottom row, Figure 3.7). For S3, the maximum variance of $S_{\omega\omega}$ is in the inner surf zone ($> 0.5L_{\mathrm{sz}}$) at large length scales (>100 m) for all elevations (Figure 3.7a), and the variance at large length scales decreases from the inner surf zone to outside of the surf zone (Figure 3.7b-d). For simulation S4, the peak eddy alongshore length scale remains near 60–100 m at all cross-shore locations (Figure 3.7e-h). For length scales of 60–100 m, the magnitude of $S_{\omega\omega}$ is largest near the outer to edge of the surf zone ($x = 0.75 - -1.0L_{\mathrm{sz}}$) in both simulations (Figure 3.7b-c,f-g).

For both simulations, the depth-varying analysis indicates that for all simulations, the spectral magnitude of $S_{\omega\omega}$ decays with depth within the surf zone, whereas there is nearly no depth variability at the edge of the surf zone and outside of the surf zone (Figure 3.7). In the outer surf zone (*i.e.*, $x = 0.75L_{\mathrm{sz}}$) of the alongshore-variable bathymetry (S3), the magnitude of $S_{\omega\omega}$ drops by over 30% over 1 m in the water column for eddy length scales ~ 80 m (Figure 3.7b), while the magnitude increases with depth by only 5% over 3 m outside of the surf zone. Notably, the magnitude of $S_{\omega\omega}$ decays with depth in the surf zone for all alongshore

length scales in S5, whereas in S3 only length scales <160 m show a decay with depth. This suggests that large eddies may be more depth dependent in the presence of bathymetric variability than for alongshore uniform bathymetry, indicating that bathymetric variability may play a role in homogenizing the largest length-scale eddies over the water column.

In the surf zone, the vorticity spectra for all simulations exhibit a peak wavenumber that varies with depth. Specifically, the peak eddy length scales in the surf zone increase with depth. For S3, in the outer surf zone ($0.75L_{sz}$), the peak length scale near-surface is $\sim$100 m and increases to $\sim$130 m at 1 m lower in the water column (Figure 3.7b). For S5, the shift in peak eddy length scale with depth is largest in the inner surf zone ($0.5L_{sz}$), where the peak eddy length scale is $\sim$70 m near-surface and increases to $\sim$90 m 0.5 m lower in the water column (Figure 3.7e). These changes of peak length scale with depth may be related to bottom boundary layer dynamics or the vertical distribution of eddy injection.

3.4   Vertical Structure of Very Low-Frequency Motion

SWASH simulations, which include vorticity generation by a range of mechanisms (*i.e.,* shear instabilities, wave-group forcing, and short-crested wave breaking vorticity injection), show depth dependence of VLF ($0.003 < f < 0.007$, Section 2.3) horizontal and rotational flow within and immediately outside of the surf zone. Here, three example transects are shown for terraced ($y = 813$ m, transecting stations p11-14) and barred ($y = 740$ m, transecting stations p21-24, Figure 3.4) beach profiles of the observed bathymetry simulation (S3) as well as the alongshore-averaged bathymetry simulation (S5) (Figure 3.8, 3.10, 3.9).

The VLF spectral density of the cross-shore and rotational velocity is highest and decreases with depth most strongly in the outer surf zone ($0.5 < L_{sz} < 1.0$) (Figure 3.8, 3.10, 3.9 a,c). The VLF alongshore velocity variance is smaller than the cross-shore variance, and is strongest near the shoreline with a weaker maximum in the outer surf zone (Figure 3.8, 3.10, 3.9 b). The horizontal and rotational velocity coherence decay with depth is largest in the outer surf zone and offshore of the surf zone for all transects (Figure 3.8, 3.10, 3.9 d-f). The alongshore uniform bathymetry (S5) exhibits a larger drop in coherence within the surf

zone than the similarly terraced observed beach profile (S3, Figure 3.8, 3.10 d-f). The barred beach profile exhibits a drop in coherence in the trough for both horizontal components of velocity and near the bar crest for the alongshore velocity (S3, Figure 3.9 d,e). Within the surf zone of all transects, the VLF cross-shore velocity phase difference from surface flows is small and most often positive, indicating a near-bottom flow that slightly leads the surface flows, whereas the alongshore velocity phase alternates sign (Figures 3.8, 3.10, 3.9 g,h). Cross-shore velocities are more variable near the surface than near the bottom onshore of the onset of wave breaking (on the terrace edge and immediately onshore of the barcrest, Figure 3.8, 3.10 3.10 j). The near-bottom VLF alongshore velocity alternates between more and less variable than the near-surface velocity for all simulations (Figure 3.8, 3.10 k).

These transects show similar depth dependence for the alongshore-averaged bathymetry (S5) and the similarly terraced observed profile (S3). The barred beach profile (S3) has the strongest vertical structure of all transects, suggesting that the presence of a deeper trough may lead to enhanced vertical variability of VLF motions. The large depth decay of coherence in the trough of the barred beach and near the outer edge of the surf zone of the terraced beach suggests that the VLF velocity is depth dependent within and immediately outside of the surf zone for both the alongshore-uniform and alongshore-varying bathymetry.

The rotary coefficient, C_R (Equation 2.14), describing the direction of dominant VLF rotation, varies vertically within the surf zone, suggesting a flow field that is turning and changing behavior with depth (Figure 3.8 3.10 3.9 l). For the majority of the surf zone, the rotary coefficient is positive (CW rotation is more energetic than the CCW rotation), which suggests that interactions with the bathymetry, waves, mean flows, or mean shear/vorticity may reinforce a particular eddy circulation direction. However, further work is needed to understand these relationships.
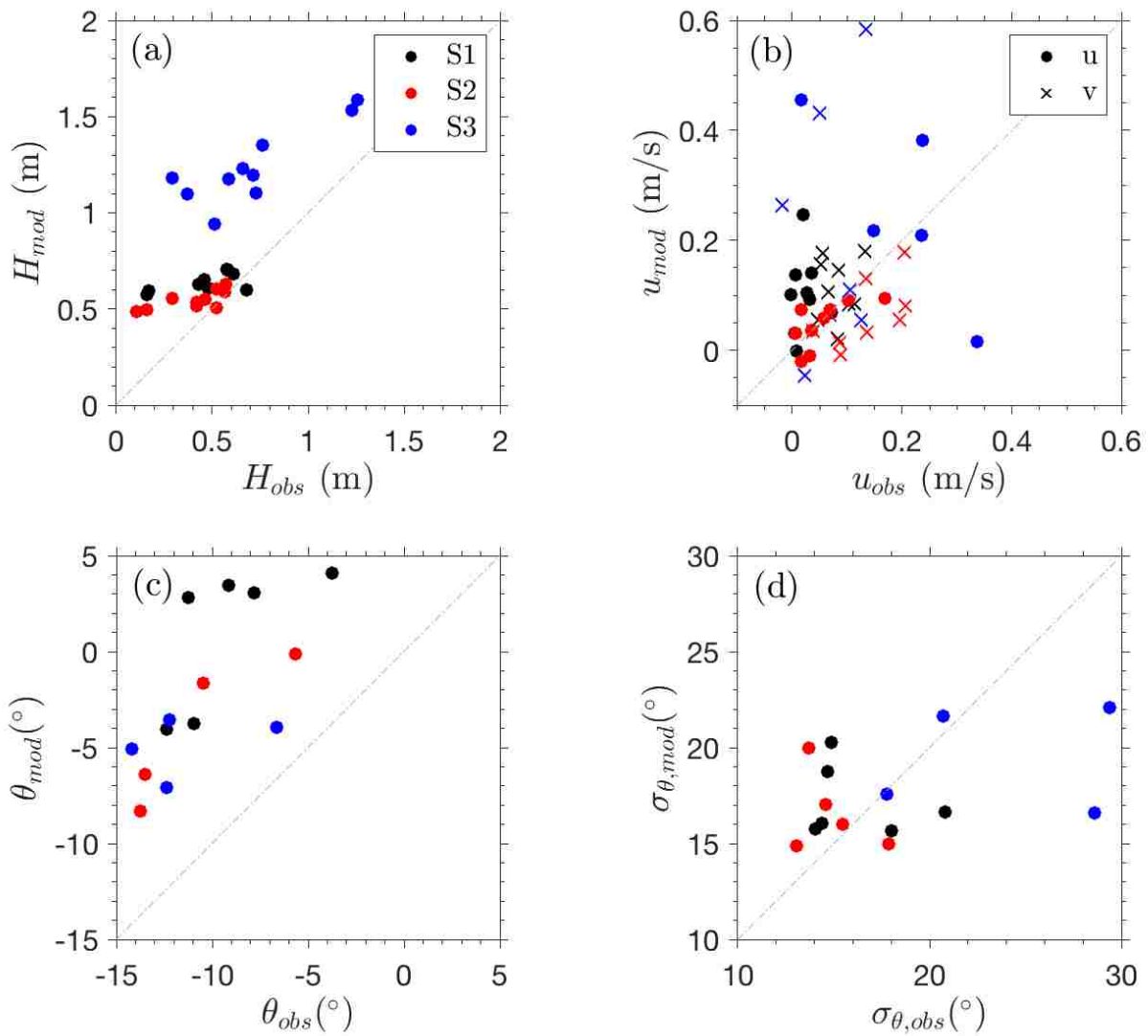
Figure 3.2: Observed (y-axis) versus modeled (x-axis) (a) significant wave height, H, (b) cross- and alongshore velocities, u and v, (c) wave incidence angle, θ, and (d) directional spread, σ_θ for simulation S1 (black), S2 (red), and S3 (blue).
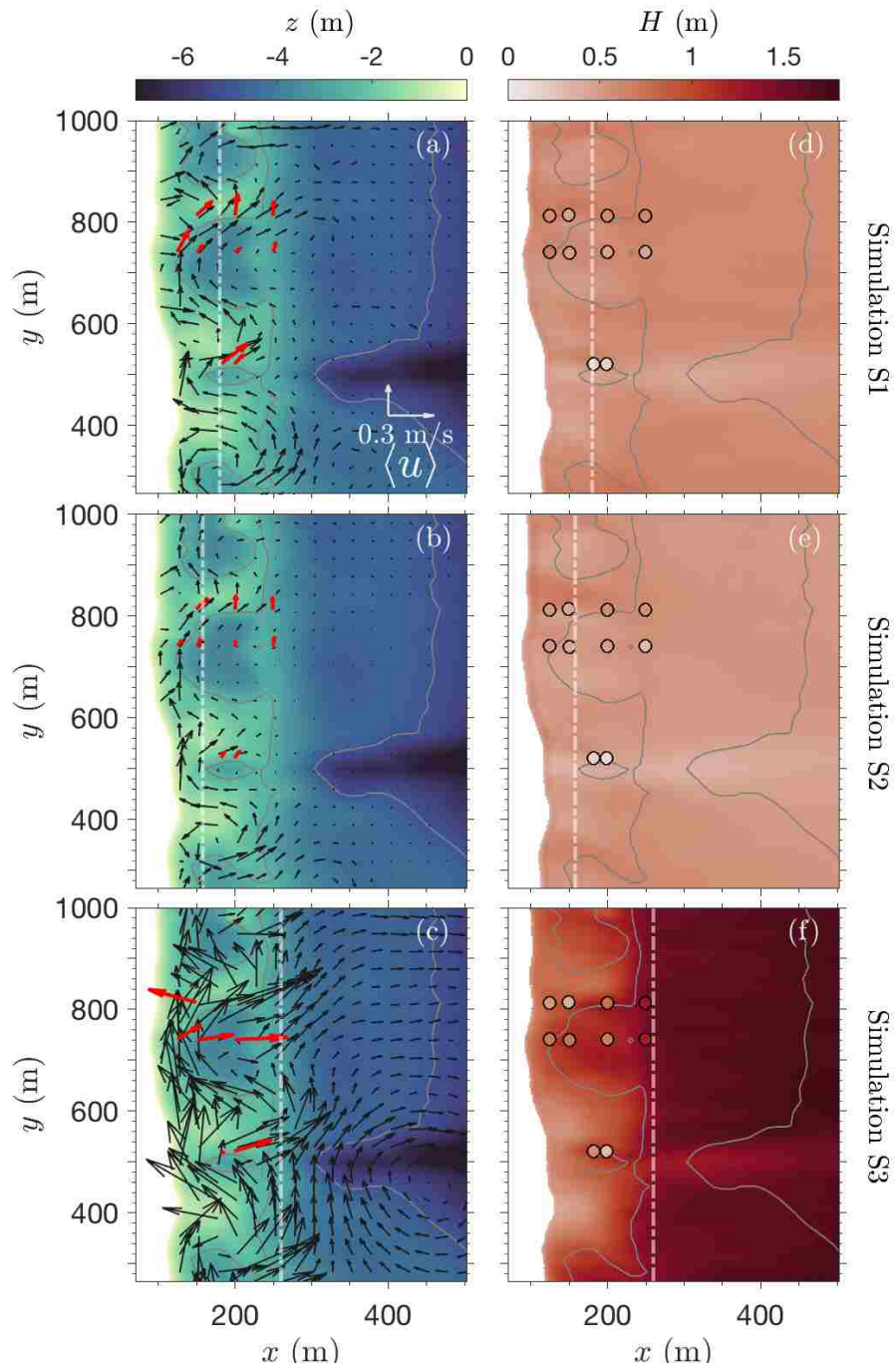
Figure 3.3: Observed (left: red arrows, right: filled circles) and modeled (left: black arrows, right: color contours) (a) significant wave height (H) and (b) time-averaged velocity ($\langle u \rangle$) over one hour for S1 (top), S2 (middle), and S3 (bottom). Bathymetry (left: color contours) and the approximate outer edge of the surf zone (all panels: dashed white line) are shown.
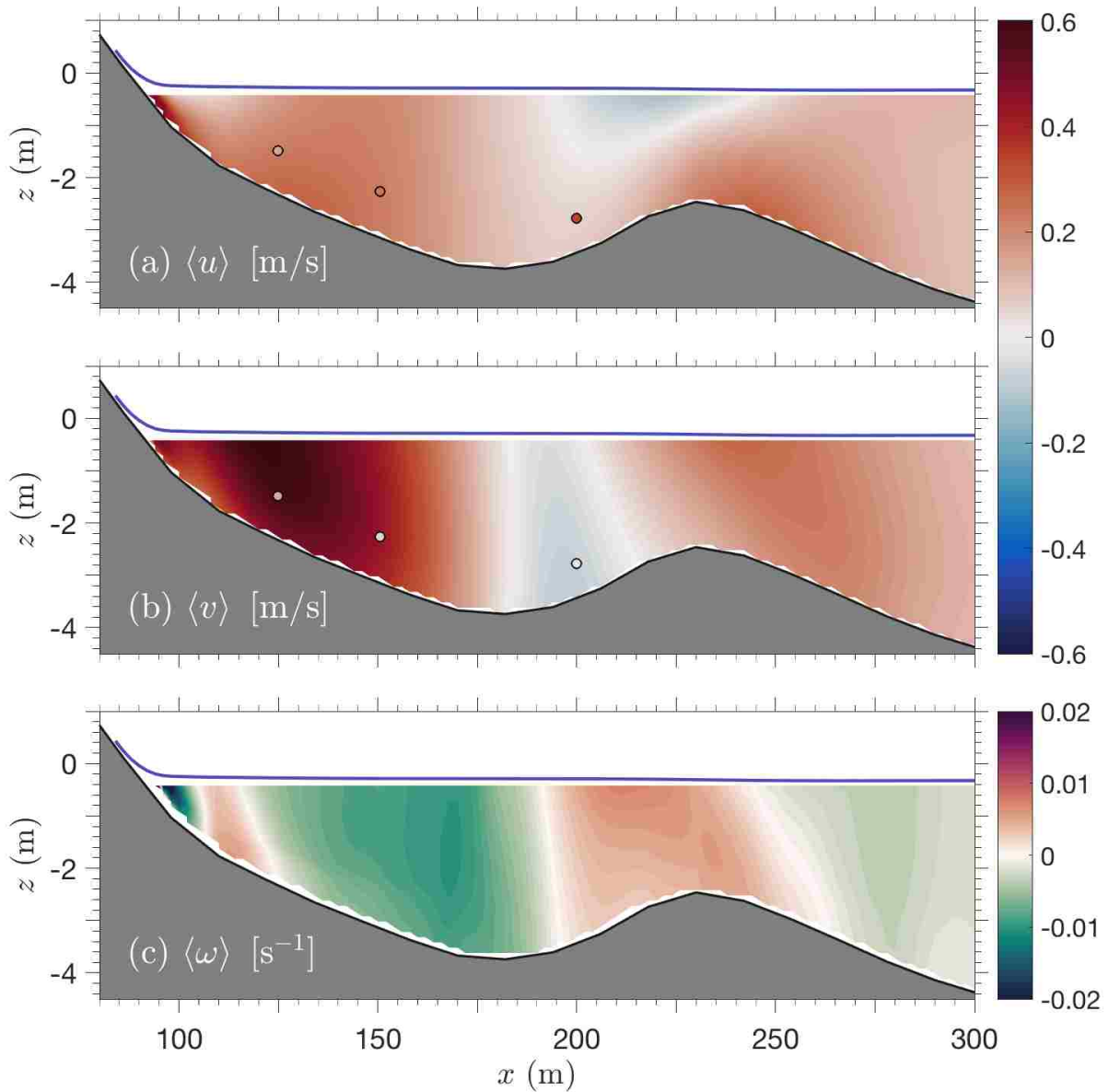
Figure 3.4: Hour-average (a) cross- and (b) alongshore velocity and (c) vorticity for observed (symbols at elevations of near-bed ADVs, p21-p23) and simulated (color contours) conditions for simulation S3 along a cross-shore transect at $y = 740$ m. Positive cross-shore velocity is offshore and positive alongshore velocity is to the north.
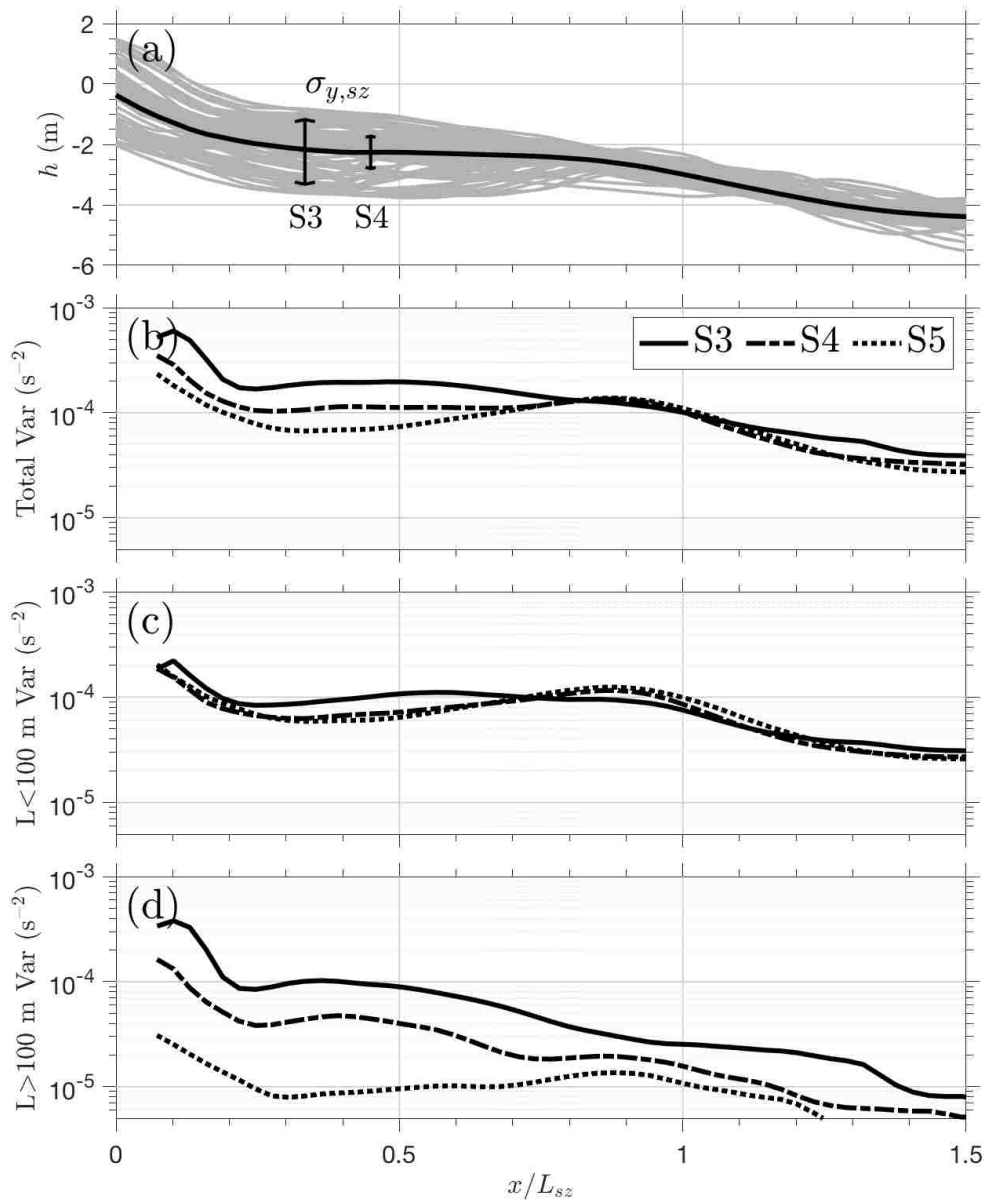
Figure 3.5: (a) The Oct 14 observed (S3, grey profiles plotted every 8-m in the alongshore) and alongshore-averaged (S5, black curve) bathymetry versus cross-shore coordinate normalized by the surfzone width. The alongshore standard deviation of the bathymetry ($\sigma_{y,sz}$) within the surf zone is denoted with arrows for S3 and S4. The variance of the alongshore wavenumber spectra of vorticity for all alongshore length scales (b) and length scales less than (c) and greater than (d) 100 m versus normalized cross-shore position for the observed bathymetry (S3, solid lines), a synthetic bathymetry with half of the observed variability (S4, dot-dashed lines), and alongshore-averaged bathymetry (S5, dashed lines).
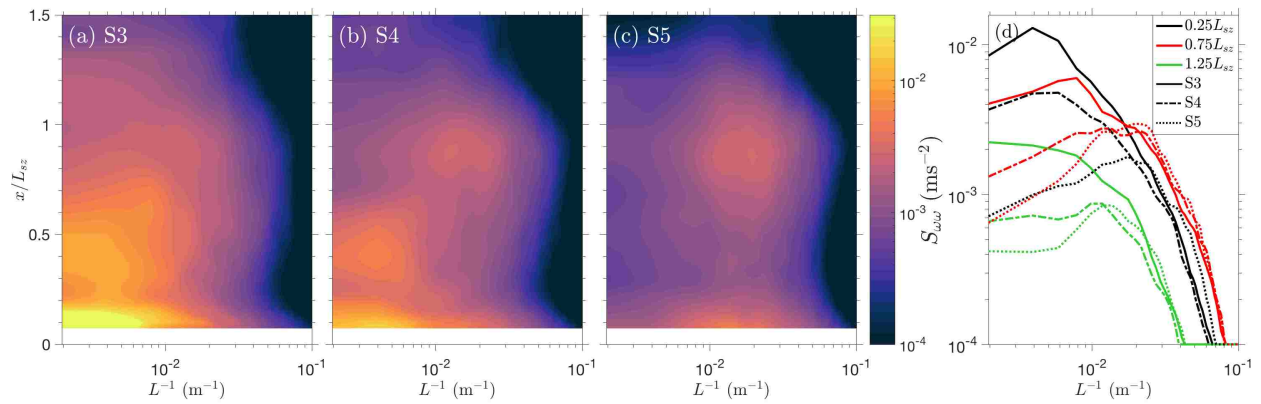
Figure 3.6: Alongshore wavenumber spectra of vorticity ($S_{\omega\omega}$, color contours) for (a) observed bathymetry (S3), (b) half of the observed bathymetric variability (S4), and (c) alongshore averaged bathymetry (S5) as a function of the normalized surfzone width x/L_{sz}, where $x/L_{sz} = 0$ is the mean shoreline and $x/L_{sz} = 1$ is the outer edge of the surf zone. The alongshore wavenumber spectra of vorticity (d) in the inner surf zone ($0.25L_{sz}$, black curves), outer surf zone ($0.75L_{sz}$, red curves), and outside of the surf zone ($1.25L_{sz}$, green curves) for S3 (solid lines), S4 (dot-dashed lines), and S5 (dotted lines).
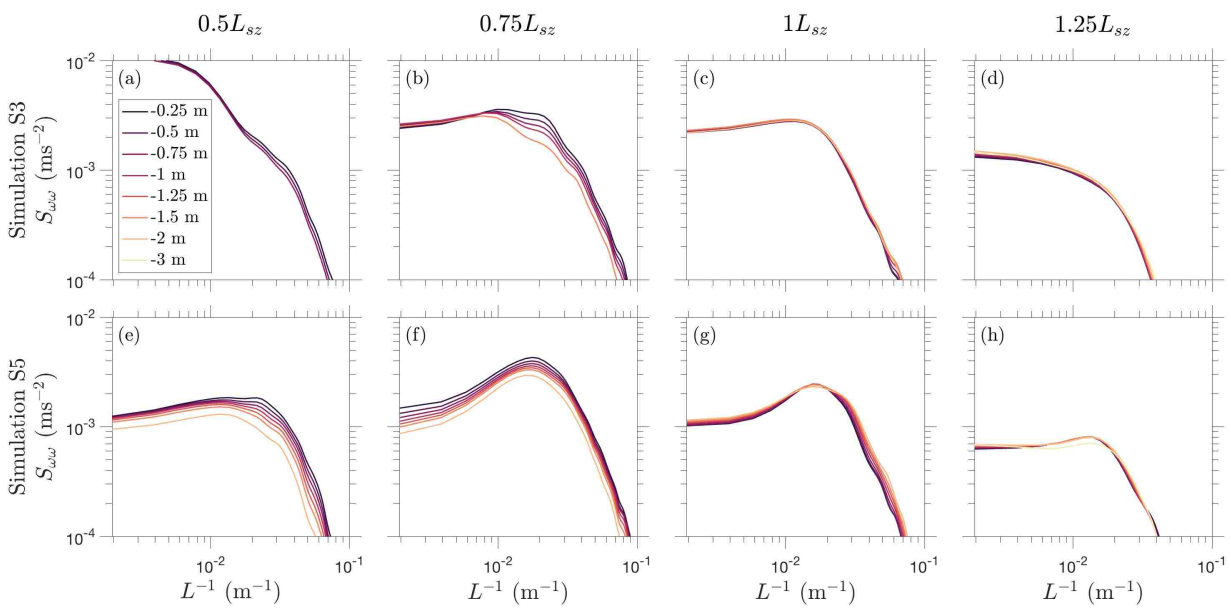
Figure 3.7: The alongshore wavenumber spectra of vorticity ($S_{\omega\omega}$) versus normalized cross-shore position at 0.25 to 3 m below the mean sea-surface elevation (colored curves, legend inset, lighter curves nearer to the bottom) for observed bathymetry (S3, top row) and alongshore-uniform bathymetry (S5, bottom row) in (a,e) the inner surf zone at $0.5L_{sz}$, (b,f) the outer surf zone at $0.75L_{sz}$, (c,g) the edge of the surf zone at $1.0L_{sz}$, and (d,h) outside of the surf zone at $1.25L_{sz}$.
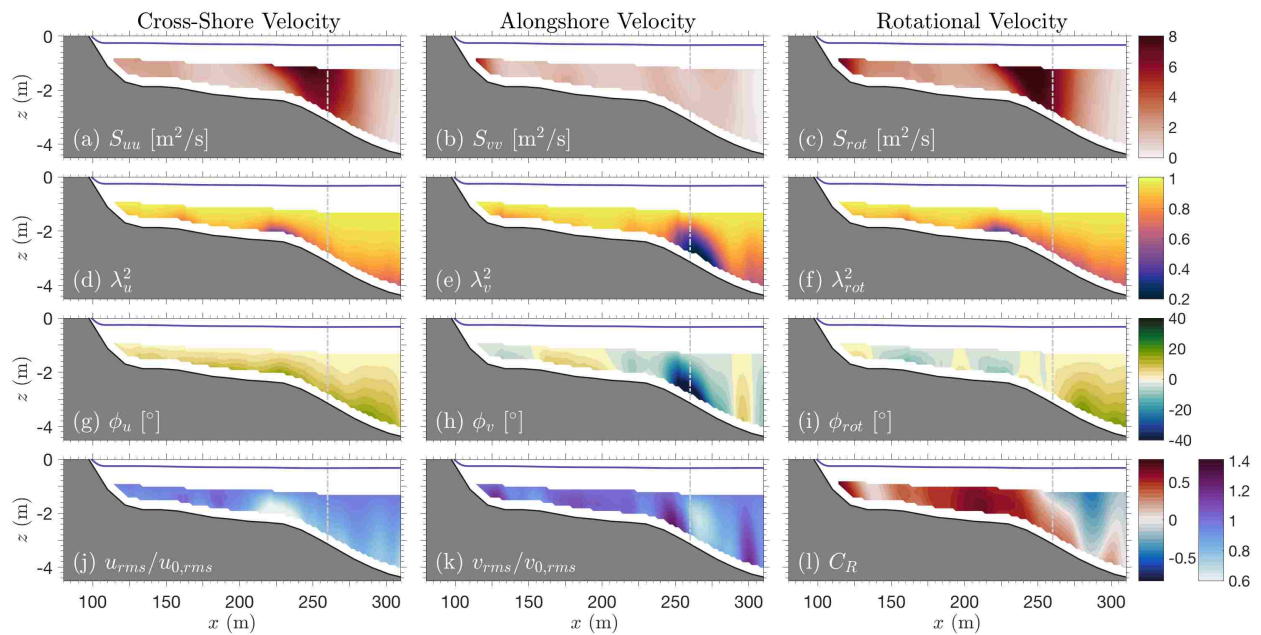
Figure 3.8: Cross-shore transect for the observed bathymetry simulation (S3) at $y = 813$ m of the cross-shore (left), alongshore (center), and rotational (right) VLF velocity spectral density (a: S_{uu}, b: S_{vv}, c: S_{rot}), squared coherence (d: λ_u^2, e: λ_v^2, f: λ_{rot}^2), phase shift (g: ϕ_u, h: ϕ_v, i: ϕ_{rot}), and the rms (j: $u_{rms}/u_{0,rms}$, k: $v_{rms}/v_{0,rms}$) relative to the rms near-surface, and the rotary coefficient (l: C_R) with the mean sea surface elevation (blue) and edge of the surf zone (dashed grey).
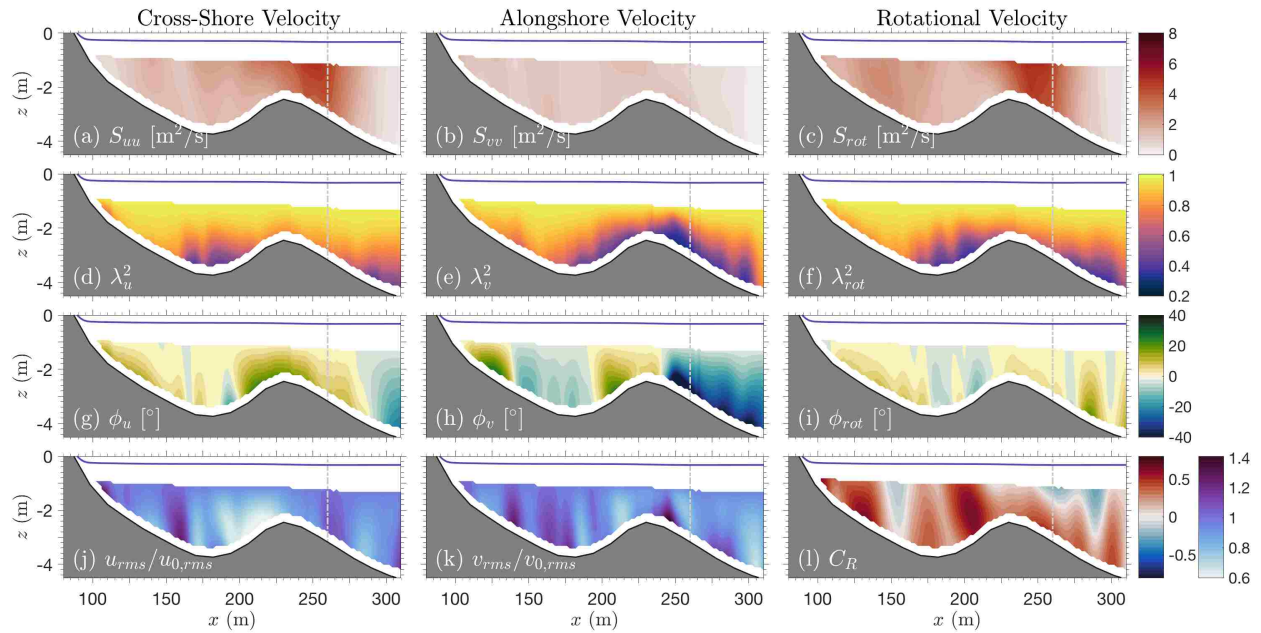
Figure 3.9: Cross-shore transect of VLF velocity parameters for a barred beach profile of the observed bathymetry (S3) at $y = 740$ m (details in Figure 3.8 caption).

Figure 3.10: Cross-shore transect of VLF velocity parameters for alongshore-uniform bathymetry (S5) at $y = 813$ m (details in Figure 3.8 caption).

Chapter 4

DISCUSSION

Previous studies have simulated surfzone circulation dynamics using depth-integrated wave-resolving Boussinesq models [*e.g.,* funwaveC, *Spydell and Feddersen*, 2009; *Kumar and Feddersen*, 2017]. For alongshore-uniform planar and barred beaches, these studies found that the alongshore wavenumber spectra of vorticity ($S_{\omega\omega}$, computed from depth-averaged velocities) is primarily red at length scales of 10–500 m, and white 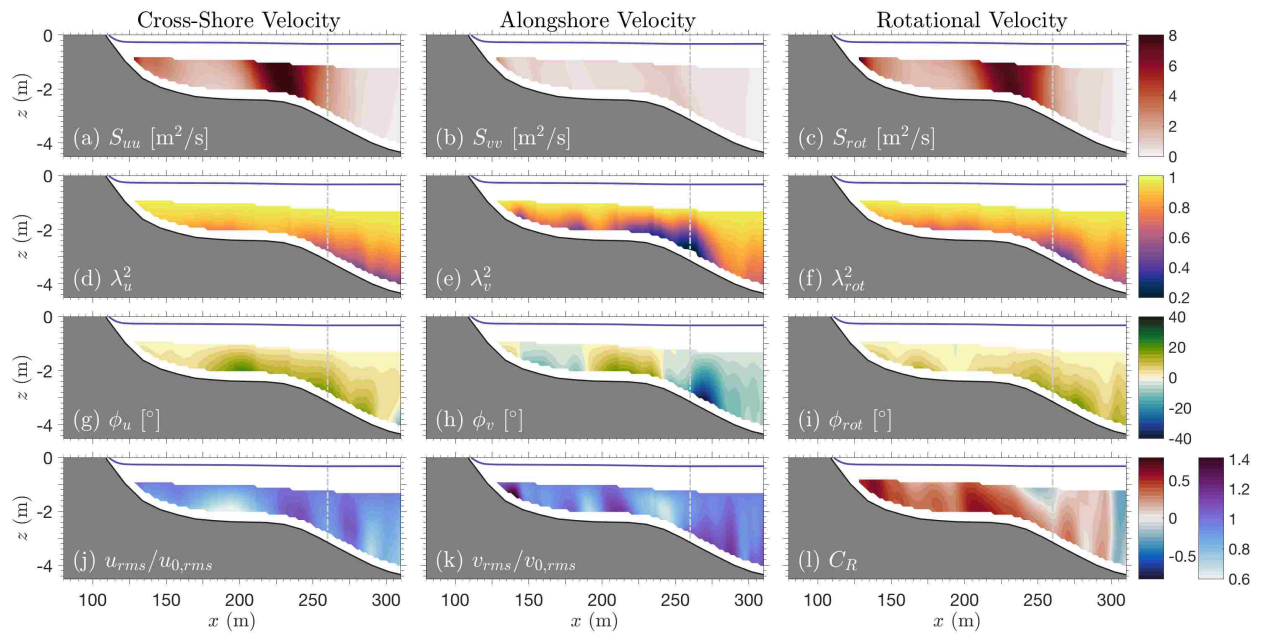at longer length scales, with a peak in $S_{\omega\omega}$ at length scales of approximately 100–500 m [*Spydell and Feddersen*, 2009; *Kumar and Feddersen*, 2017]. For the range of bathymetry patterns simulated here (Figure 3.5a), the vorticity spectrum in the surf zone has a similar shape to these previous studies (Figure 3.6), however, the peak in $S_{\omega\omega}$ occurs at smaller length scales (60–100 m), and a decrease in energy at larger length scales occurs for the alongshore uniform simulation. In a previous study using a wave-averaged linear wave group model with alongshore homogenous bathymetry, VLF eddy alongshore length scales were found to be O(50-1000)m, however this modeling approach neglects nonlinear energy transfers [*MacMahan et al.*, 2010]. The alongshore length scales in the alongshore-uniform simulation (S5) overlap with this range, however, here the variance is concentrated between length scales of 60–100 m (Figure 3.6).

In a previous study that analyzed drifter trajectories observed in the surf zone and simulated surfzone flows with a Boussinesq model, the magnitude of the alongshore wavenumber spectra of vorticity was found to be dependent on wave field directional spread for an alongshore uniform beach with shore-normal waves [*Spydell and Feddersen*, 2009]. While the dependence on wave conditions was not explored in detail here, the similar roll off and magnitude of $S_{\omega\omega}$ at shorter length scales for several simulations with the same wave forcing and a range of bathymetry variability (*e.g.,* S3, S4, and S5) is consistent with previous results
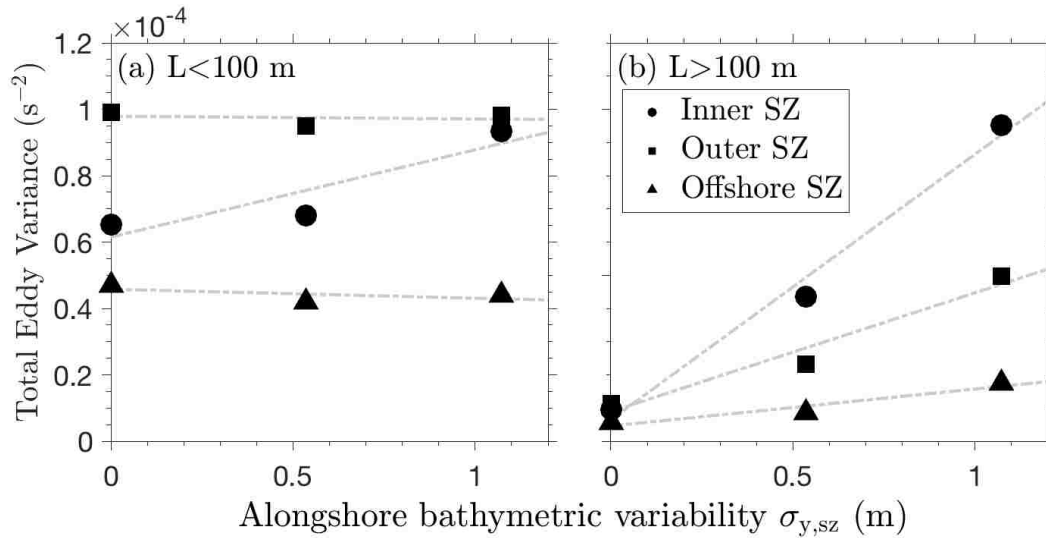
Figure 4.1: The average total variance of small (a, L<100 m) and large (b,L>100 m) eddy length scales for the inner surf zone (SZ) (circles, $0.2< x/L_{sz} <0.5$), outer surf zone (squares, $0.5< x/L_{sz} <1$), and offshore of the surf zone (triangles, $1< x/L_{sz} <1.5$) versus the along-shore standard deviation of surfzone bathymetric variability for each simulation (S3, S4, S5). A linear fit is shown for each region (grey dashed lines).

that variance at these scales may be controlled by the incident wave field (Figure 3.6). Short-crested directionally spread waves, such as the wave conditions in the simulations here, inject vorticity during breaking at length scales >20 m, which may be transferred to longer length scales through an inverse cascade or dissipated through bottom friction [*Kraichnan*, 1967; *Rutgers*, 1998; *Boffetta and Ecke*, 2012]. In addition to short-crested wave eddy generation, wave-group driven alongshore radiation stress gradients from alongshore wave breaking vari-ability may contribute to the total variance at small eddy length scales [*Haller et al.*, 1999; *Long and Özkan Haller*, 2009].

While previous studies have investigated the role of wave directional spread and wave groups in VLF eddy variance, the role of bathymetric variability had not been investigated in detail. Here, the variance and length scales of eddies in the inner surf zone ($0.2< x/L_{sz} <0.5$), outer surf zone ($0.5< x/L_{sz} <1$), and offshore of the surf zone ($1< x/L_{sz} <1.5$) are related

to the maximum alongshore standard deviation of the bathymetry in three simulations with the same wave forcing and different bathymetric variability (S3, S4, S5, Figure 4.1). The maximum total variance of small eddies (L¡100 m) occurs in the outer surf zone, a location corresponding to maximum wave dissipation (Figure 4.1a, squares). The total variance of small length-scale eddies is independent of bathymetric variability offshore of the surf zone and at the outer edge of the surf zone (triangles, squares, and linear fits with slopes = -0.04×10^{-4} and $-0.01 \times 10^{-4} \mathrm{m}^{-1}\mathrm{s}^{-2}$, respectively), consistent with previous studies showing the variance of small length scales is dependent on wave conditions. In the inner surf zone, the variance of small length-scale eddies exhibits a moderate dependence on bathymetric variability (slope = 0.41×10^{-4} $\mathrm{m}^{-1}\mathrm{s}^{-2}$).

In contrast, the eddy variance at large length scales (L>100 m) increases strongly with alongshore bathymetric variability in the inner surf zone (Figure 4.1b, circles and linear fit with slope = 1.26×10^{-4} $\mathrm{m}^{-1}\mathrm{s}^{-2}$). There is a weaker increase of eddy variance with bathymetric variability in the outer surf zone and offshore of the surf zone (slopes = 0.56×10^{-4} and 0.17×10^{-4} $\mathrm{m}^{-1}\mathrm{s}^{-2}$, respectively). The intensified generation of large-scale eddies in the simulations with larger bathymetric variance may be due to the presence of alongshore varying bathymetric features (Figure 3.5a), including deep troughs where eddies may coalesce [*Kraichnan*, 1967; *Rutgers*, 1998; *Boffetta and Ecke*, 2012]. Bathymetric features such as deeper troughs may enhance eddy rotational speeds due to reduced bottom friction in larger water depths, eddy acceleration when entering deeper regions, and trapping of eddies in troughs [*Bhler and Jacobson*, 2001]. In addition, the highly variable observed bathymetry modulates wave breaking patterns, driving meandering mean flow patterns (Figure 3.3c), which may pulsate at very low frequencies including wave-group timescales and may shed large eddies due to shear instabilities [*MacMahan et al.*, 2004a; *Reniers et al.*, 2007; *Geiman and Kirby*, 2013]. Previous simulations with a wave-averaged wave-current model also have indicated that bathymetric variability is an important factor in intensifying eddy kinetic energy [*Uchiyama et al.*, 2017]. The presence of alongshore inhomogeneous bathymetry, which causes variable wave breaking and meandering mean circulation, may be associated

with complex nonlinear interactions between eddies of different length scales, mean flows, and bathymetry that may modify eddy length scales or reinforce a specific eddy rotational direction.

While previous studies have quantified surfzone eddy variability with alongshore arrays of electromagnetic current meters at one elevation in the water column [*Oltman-Shay et al.*, 1989; *Noyes*, 2004], the depth variability of eddies in the surf zone has been investigated in only a few studies, and no previous numerical modeling experiments have investigated the depth variability of vortical motion with a fully 3D phase-resolving model. Model simulations using a quasi-3D phase-averaged model exhibited vertical structure of shear instabilities [*Zhao et al.*, 2003], however, this model assumes regular waves and does not account for wave-forced eddy generation, which may be an important source of eddy energy, and thus, may play a role in the vertical structure of eddies [*Zhao et al.*, 2003; *Newberger and Allen*, 2007].

Recent field studies investigating the vertical structure of vortical motion on a barred beach found significant vertical structure [*Lippmann et al.*, 2016; *Henderson et al.*, 2017]. Consistent with observations, the SWASH simulated spectral energy of the VLF cross-shore velocity at the seaward side of the bar crest decays with depth and the coherence drops by as much as 80% within the water column [*Lippmann et al.*, 2016]. While prior studies noted that phase shifts increased with decreasing coherence [*Lippmann et al.*, 2016], no clear relationship between the coherence and phase is evident here. Near-bottom velocities both led and lagged near-surface velocities within the surf zone of SWASH simulations, consistent with previous work [*Henderson et al.*, 2017], suggesting that inconsistent phase relationships documented in different observational studies [*Lippmann et al.*, 2016; *Henderson et al.*, 2017] may be due to differing bathymetric condition and the limited number of wave conditions sampled.

SWASH simulations are consistent with previous results that identified strong depth dependence of eddies immediately outside of the surf zone [*Henderson et al.*, 2017; *Lippmann et al.*, 2016]. In contrast to prior observations, SWASH simulations show significant vertical

structure within the trough of a barred beach (Figure 3.9) and during strong wave conditions [*Lippmann et al.*, 2016; *Henderson et al.*, 2017]. The vertical structure of eddies in the surf zone may result from instabilities and bottom boundary layer dynamics, as previously proposed with a theoretical model for eddy depth dependence in the presence of a depth-uniform alongshore mean current [*Lippmann and Bowen*, 2016]. These solutions, which include bottom friction and linearized lateral momentum advection, suggest that eddy vertical structure may depend on vertical mixing, eddy scales, and the magnitude of shear from an alongshore current, but do not address the role of variability in wave forcing in a phase-resolved framework.

Here, the SWASH simulations indicate complex horizontal and vertical structure of vortical motions that have not been resolved in most previous modeling and observational studies. The simulated eddy variance decays with depth (magnitude of $S_{\omega\omega}$) and exhibits an increase in the peak eddy length scale with depth (Figure 3.7), indicating that eddies are depth dependent within the surf zone for both bathymetrically variable and uniform beaches. Furthermore, horizontal and rotational very low-frequency (VLF) velocity components have significant depth dependence for simulations with and without alongshore bathymetric variability. These results suggest that the depth dependence of surfzone eddies may be important, and thus, indicate that measurements characterizing surfzone eddies may be sensitive to the vertical position of the sensor, even in the absence of alongshore bathymetric variability. Further investigation is necessary to understand the complex three-dimensional structure of VLF motion in the surf zone, including the sensitivity to a variety of wave and bathymetry conditions, and the implications for cross-shore exchange.

Chapter 5

CONCLUSIONS

Three-dimensional circulation patterns and resulting mixing and dispersion of tracer in the nearshore are sensitive to the three-dimensionality of eddies generated in the surf zone, however few studies have investigated three-dimensional surfzone eddies, and no previous studies have investigated these dynamics in three-dimensional phase-resolving model. In this study, a three-dimensional phase-resolving model, SWASH, is used to simulate surface wave transformation and circulation patterns on an alongshore-inhomogeneous barred beach at Duck, NC. Model simulations reproduce the magnitudes and patterns of the observed wave statistics and nearshore flows with reasonable skill for three test cases with directionally spread shore-normal and obliquely incident waves. Observed spatial patterns, including the cross-shore wave height gradient, the mean alongshore currents, and the meandering circulation features are reproduced in simulations with obliquely incident waves (S1, S2). Differences between modeled and observed spatial patterns for shore-normal waves (S3) may be related to inaccuracies in the bathymetry.

The three-dimensional simulations illustrate the complex spatial structure of vortical motion in the surf zone. Eddy length scales quantified using the alongshore wavenumber spectra of vorticity, $S_{\omega\omega}$, suggest that intensified formation of large alongshore length-scale eddies, $\mathcal{O}(100)$ may increase with bathymetric variability. The variance of small length-scale eddies, $\mathcal{O}(10)$ m is independent of alongshore bathymetric variability in the outer surf zone and just offshore of the surf zone, suggesting that vortical motion with short alongshore length scales may be related to the incident wave field (i.e., wave forced by wave groups and short-crested wave breaking).

With and without bathymetric variability, modeled eddy energy and peak length scales

are depth dependent, and the horizontal and vertical structure of very low-frequency (VLF) motions have complex patterns. Further investigation is necessary to understand the complex three-dimensional VLF vertical and horizontal variability in the surf zone.

BIBLIOGRAPHY

Allen, J. S., P. A. Newberger, and R. A. Holman, Nonlinear shear instabilities of along-shore currents on plane beaches, *Journal of Fluid Mechanics*, *310*, 181–213, doi:10.1017/S0022112096001772, 1996.

Boehm, A. B., N. S. Ismail, L. M. Sassoubre, and E. A. Andruszkiewicz, Oceans in Peril: Grand Challenges in Applied Water Quality Research for the 21st Century, *Environmental Engineering Science*, *34*(1), 3–15, doi:10.1089/ees.2015.0252, 2017.

Boffetta, G., and R. E. Ecke, Two-Dimensional Turbulence, *Annual Review of Fluid Mechanics*, *44*(1), 427–451, doi:10.1146/annurev-fluid-120710-101240, 2012.

Bonneton, P., N. Bruneau, B. Castelle, and F. Marche, Large-scale vorticity generation due to dissipating waves in the surf zone, *Discrete and Continuous Dynamical Systems - Series B*, *13*(4), 729–738, doi:10.3934/dcdsb.2010.13.729, 2010.

Bowen, A. J., and R. T. Guza, Edge waves and surf beat, *Journal of Geophysical Research: Oceans*, *83*(C4), 1913–1920, doi:10.1029/JC083iC04p01913, 1978.

Bowen, A. J., and R. A. Holman, Shear instabilities of the mean longshore current: 1. Theory, *Journal of Geophysical Research: Oceans*, *94*(C12), 18,023–18,030, doi:10.1029/JC094iC12p18023, 1989.

Bowen, A. J., D. L. Inman, and V. P. Simmons, Wave set-down and set-Up, *Journal of Geophysical Research*, *73*(8), 2569–2577, doi:10.1029/JB073i008p02569, 1968.

Bhler, O., and T. E. Jacobson, Wave-driven currents and vortex dynamics on barred beaches, *Journal of Fluid Mechanics*, *449*, 313–339, doi:10.1017/S0022112001006322, 2001.

Clark, D. B., F. Feddersen, and R. T. Guza, Cross-shore surfzone tracer dispersion in an alongshore current, *Journal of Geophysical Research: Oceans*, *115*(C10), doi: 10.1029/2009JC005683, 2010.

Clark, D. B., F. Feddersen, and R. T. Guza, Modeling surf zone tracer plumes: 2. Transport and dispersion, *Journal of Geophysical Research: Oceans*, *116*(C11), doi: 10.1029/2011JC007211, 2011.

Clark, D. B., S. Elgar, and B. Raubenheimer, Vorticity generation by short-crested wave breaking, *Geophysical Research Letters*, *39*(24), doi:10.1029/2012GL054034, 2012.

Dalrymple, R. A., J. H. MacMahan, A. J. Reniers, and V. Nelko, Rip Currents, *Annual Review of Fluid Mechanics*, *43*(1), 551–581, doi:10.1146/annurev-fluid-122109-160733, 2011.

de Bakker, A. T. M., M. F. S. Tissier, and B. G. Ruessink, Beach steepness effects on nonlinear infragravitywave interactions: A numerical study, *Journal of Geophysical Research: Oceans*, *121*(1), 554–570, doi:10.1002/2015JC011268, 2016.

Dodd, N., J. Oltman-Shay, and E. B. Thornton, Shear Instabilities in the Longshore Current: A Comparison of Observation and Theory, *Journal of Physical Oceanography*, *22*(1), 62–82, doi:10.1175/1520-0485(1992)022⟨0062:SIITLC⟩2.0.CO;2, 1992.

Eckart, C., Surface waves on water of variable depth, *Wave report nr. 100, SIO reference 51-12*, 1951.

Elgar, S., and R. T. Guza, Observations of bispectra of shoaling surface gravity waves, *Journal of Fluid Mechanics*, *161*, 425–448, doi:10.1017/S0022112085003007, 1985.

Elgar, S., B. Raubenheimer, and R. T. Guza, Quality control of acoustic Doppler velocimeter data in the surfzone, *Measurement Science and Technology*, *16*(10), 1889–1893, doi:10. 1088/0957-0233/16/10/002, 2005.

Elgar, S., B. Raubenheimer, D. B. Clark, and M. Moulton, Extremely Low Frequency (0.1 to 1.0 mHz) Surf Zone Currents, *Geophysical Research Letters*, *46*(3), 1531–1536, doi: 10.1029/2018GL081106, 2019.

Feddersen, F., Weakly nonlinear shear waves, *Journal of Fluid Mechanics*, *372*, 71–91, doi: 10.1017/S0022112098002158, 1998.

Feddersen, F., The Generation of Surfzone Eddies in a Strong Alongshore Current, *Journal of Physical Oceanography*, *44*(2), 600–617, doi:10.1175/JPO-D-13-051.1, 2014.

Feddersen, F., R. T. Guza, S. Elgar, and T. H. C. Herbers, Alongshore momentum balances in the nearshore, *Journal of Geophysical Research: Oceans*, *103*(C8), 15,667–15,676, doi: 10.1029/98JC01270, 1998.

Feddersen, F., D. B. Clark, and R. T. Guza, Modeling surf zone tracer plumes: 1. Waves, mean currents, and low-frequency eddies, *Journal of Geophysical Research*, *116*(C11), doi: 10.1029/2011JC007210, 2011.

Garcez-Faria, A. F., E. B. Thornton, T. P. Stanton, C. V. Soares, and T. C. Lippmann, Vertical profiles of longshore currents and related bed shear stress and bottom roughness, *Journal of Geophysical Research: Oceans*, *103*(C2), 3217–3232, doi:10.1029/97JC02265, 1998.

Garcez-Faria, A. F., E. B. Thornton, T. C. Lippmann, and T. P. Stanton, Undertow over a barred beach, *Journal of Geophysical Research: Oceans*, *105*(C7), 16,999–17,010, doi: 10.1029/2000JC900084, 2000.

Geiman, J. D., and J. T. Kirby, Unforced Oscillation of Rip-Current Vortex Cells, *Journal of Physical Oceanography*, *43*(3), 477–497, doi:10.1175/JPO-D-11-0164.1, 2013.

Gonella, J., A rotary-component method for analysing meteorological and oceanographic vector time series, *Deep Sea Research and Oceanographic Abstracts*, *19*(12), 833–846, doi: 10.1016/0011-7471(72)90002-2, 1972.

Guza, R. T., and E. B. Thornton, Local and shoaled comparisons of sea surface elevations, pressures, and velocities, *Journal of Geophysical Research: Oceans*, *85*(C3), 1524–1530, doi:10.1029/JC085iC03p01524, 1980.

Guza, R. T., and E. B. Thornton, Observations of surf beat, *Journal of Geophysical Research: Oceans*, *90*(C2), 3161–3172, doi:10.1029/JC090iC02p03161, 1985.

Haller, M. C., U. Putrevu, J. Oltman-Shay, and R. A. Dalrymple, Wave group forcing of low frequency surf zone motion, *Coastal engineering journal*, *41*(02), 121–136, 1999.

HallyRosendahl, K., and F. Feddersen, Modeling surfzone to inner-shelf tracer exchange, *Journal of Geophysical Research: Oceans*, *121*(6), 4007–4025, doi:10.1002/2015JC011530, 2016.

Henderson, S. M., J. Arnold, H. T. zkanHaller, and S. A. Solovitz, Depth Dependence of Nearshore Currents and Eddies, *Journal of Geophysical Research: Oceans*, *122*(11), 9004–9031, doi:10.1002/2016JC012349, 2017.

Johnson, D., and C. Pattiaratchi, Boussinesq modelling of transient rip currents, *Coastal Engineering*, *53*(5), 419–439, doi:10.1016/j.coastaleng.2005.11.005, 2006.

Kraichnan, R. H., Inertial Ranges in TwoDimensional Turbulence, *The Physics of Fluids*, *10*(7), 1417–1423, doi:10.1063/1.1762301, 1967.

Kumar, N., and F. Feddersen, The Effect of Stokes Drift and Transient Rip Currents on the Inner Shelf. Part I: No Stratification, *Journal of Physical Oceanography*, *47*(1), 227–241, doi:10.1175/JPO-D-16-0076.1, 2017.

Kumar, N., G. Voulgaris, J. C. Warner, and M. Olabarrieta, Implementation of the vortex force formalism in the coupled ocean-atmosphere-wave-sediment transport (COAWST) modeling system for inner shelf and surf zone applications, *Ocean Modelling*, *47*, 65–95, doi:10.1016/j.ocemod.2012.01.003, 2012.

Lam, D. C. L., and R. B. Simpson, Centered differencing and the box scheme for diffusion convection problems, *Journal of Computational Physics*, *22*(4), 486–500, doi: 10.1016/0021-9991(76)90045-0, 1976.

Lippmann, T. C., and A. J. Bowen, The Vertical Structure of Low-Frequency Motions in the Nearshore. Part II: Theory, *Journal of Physical Oceanography*, *46*(12), 3713–3727, doi:10.1175/JPO-D-16-0015.1, 2016.

Lippmann, T. C., E. B. Thornton, and T. P. Stanton, The Vertical Structure of Low-Frequency Motions in the Nearshore. Part I: Observations, *Journal of Physical Oceanography*, *46*(12), 3695–3711, doi:10.1175/JPO-D-16-0014.1, 2016.

Long, J. W., and H. T. Özkan Haller, Low-frequency characteristics of wave groupforced vortices, *Journal of Geophysical Research*, *114*(C8), doi:10.1029/2008JC004894, 2009.

Long, J. W., and H. T. ÖzkanHaller, Offshore controls on nearshore rip currents, *Journal of Geophysical Research: Oceans*, *110*(C12), doi:10.1029/2005JC003018, 2005.

Longuet-Higgins, M. S., Longshore currents generated by obliquely incident sea waves: 1, *Journal of Geophysical Research (1896-1977)*, *75*(33), 6778–6789, doi:10.1029/JC075i033p06778, 1970.

Longuet-Higgins, M. S., A model of flow separation at a free surface, *Journal of Fluid Mechanics*, *57*(1), 129–148, doi:10.1017/S0022112073001060, 1973.

Longuet-Higgins, M. S., and R. w. Stewart, Radiation stresses in water waves; a physical discussion, with applications, *Deep Sea Research and Oceanographic Abstracts*, *11*(4), 529–562, doi:10.1016/0011-7471(64)90001-4, 1964.

Lynett Patrick J., Nearshore Wave Modeling with High-Order Boussinesq-Type Equations, *Journal of Waterway, Port, Coastal, and Ocean Engineering*, *132*(5), 348–357, doi:10.1061/(ASCE)0733-950X(2006)132:5(348), 2006.

MacMahan, J. H., A. J. H. M. Reniers, E. B. Thornton, and T. P. Stanton, Infragravity rip current pulsations, *Journal of Geophysical Research: Oceans*, *109*(C1), doi:10.1029/2003JC002068, 2004a.

MacMahan, J. H., A. J. H. M. Reniers, E. B. Thornton, and T. P. Stanton, Surf zone eddies coupled with rip current morphology, *Journal of Geophysical Research: Oceans*, *109*(C7), doi:10.1029/2003JC002083, 2004b.

MacMahan, J. H., E. B. Thornton, and A. J. H. M. Reniers, Rip current review, *Coastal Engineering*, *53*(2), 191–208, doi:10.1016/j.coastaleng.2005.10.009, 2006.

MacMahan, J. H., A. J. H. M. Reniers, and E. B. Thornton, Vortical surf zone velocity fluctuations with 0(10) min period, *Journal of Geophysical Research*, *115*(C6), C06,007, doi:10.1029/2009JC005383, 2010.

Newberger, P. A., and J. S. Allen, Forcing a three-dimensional, hydrostatic, primitive-equation model for application in the surf zone: 2. Application to DUCK94, *Journal of Geophysical Research: Oceans*, *112*(C8), doi:10.1029/2006JC003474, 2007.

Noyes, T. J., Field observations of shear waves in the surf zone, *Journal of Geophysical Research*, *109*(C1), doi:10.1029/2002JC001761, 2004.

Okey, N., Alternative Form of Boussinesq Equations for Nearshore Wave Propagation, *Journal of Waterway, Port, Coastal, and Ocean Engineering*, *119*(6), 618–638, doi:10.1061/(ASCE)0733-950X(1993)119:6(618), 1993.

Oltman-Shay, J., P. A. Howd, and W. A. Birkemeier, Shear instabilities of the mean longshore current: 2. Field observations, *Journal of Geophysical Research: Oceans*, *94*(C12), 18,031–18,042, doi:10.1029/JC094iC12p18031, 1989.

ÖzkanHaller, H. T., and Y. Li, Effects of wave-current interaction on shear instabilities of longshore currents, *Journal of Geophysical Research: Oceans*, *108*(C5), doi:10.1029/2001JC001287, 2003.

Patankar, S. V., Numerical heat transfer and fluid flow, hemisphere publ, *Corp., New York*, *58*, 1980.

Peregrine, D., Surf Zone Currents, *Theoretical and Computational Fluid Dynamics*, *10*(1), 295–309, doi:10.1007/s001620050065, 1998.

Peregrine, D. H., Water waves, nonlinear Schrdinger equations and their solutions, *The ANZIAM Journal*, *25*(1), 16–43, doi:10.1017/S0334270000003891, 1983.

Peregrine, D. H., Large-scale vorticity generation by breakers in shallow and deep water, *European Journal of Mechanics - B/Fluids*, *18*(3), 403–408, doi:10.1016/S0997-7546(99) 80037-5, 1999.

Pineda, J., J. A. Hare, and S. Sponaugle, Larval Transport and Dispersal in the Coastal Ocean and Consequences for Population Connectivity, *Oceanography*, *20*(3), 22–39, 2007.

Putrevu, U., J. OltmanShay, and I. A. Svendsen, Effect of alongshore nonuniformities on longshore current predictions, *Journal of Geophysical Research: Oceans*, *100*(C8), 16,119–16,130, doi:10.1029/95JC01459, 1995.

Raubenheimer, B., R. T. Guza, and S. Elgar, Field observations of wave-driven setdown and setup, *Journal of Geophysical Research: Oceans*, *106*(C3), 4629–4638, doi:10.1029/ 2000JC000572, 2001.

Reniers, A. J. H. M., J. A. Roelvink, and E. B. Thornton, Morphodynamic modeling of an embayed beach under wave group forcing, *Journal of Geophysical Research: Oceans*, *109*(C1), doi:10.1029/2002JC001586, 2004a.

Reniers, A. J. H. M., E. B. Thornton, T. P. Stanton, and J. A. Roelvink, Vertical flow structure during Sandy Duck: observations and modeling, *Coastal Engineering*, *51*(3), 237–260, doi:10.1016/j.coastaleng.2004.02.001, 2004b.

Reniers, A. J. H. M., J. H. MacMahan, E. B. Thornton, and T. P. Stanton, Modeling of very low frequency motions during RIPEX, *Journal of Geophysical Research: Oceans*, *112*(C7), doi:10.1029/2005JC003122, 2007.

Reniers, A. J. H. M., J. H. MacMahan, E. B. Thornton, T. P. Stanton, M. Henriquez, J. W. Brown, J. A. Brown, and E. Gallagher, Surf zone surface retention on a rip-channeled beach, *Journal of Geophysical Research: Oceans*, *114*(C10), doi:10.1029/2008JC005153, 2009.

Rijnsdorp, D. P., P. B. Smit, and M. Zijlema, Non-hydrostatic modelling of infragravity waves using swash, *Coastal Engineering Proceedings*, *1*(33), 27, doi:10.9753/icce.v33.currents.27, 2012.

Rijnsdorp, D. P., P. B. Smit, and M. Zijlema, Non-hydrostatic modelling of infragravity waves under laboratory conditions, *Coastal Engineering*, *85*, 30–42, doi:10.1016/j.coastaleng.2013.11.011, 2014.

Ruju, A., J. L. Lara, and I. J. Losada, Numerical analysis of run-up oscillations under dissipative conditions, *Coastal Engineering*, *86*, 45–56, doi:10.1016/j.coastaleng.2014.01.010, 2014.

Rutgers, M. A., Forced 2d Turbulence: Experimental Evidence of Simultaneous Inverse Energy and Forward Enstrophy Cascades, *Physical Review Letters*, *81*(11), 2244–2247, doi:10.1103/PhysRevLett.81.2244, 1998.

Shanks, A. L., S. G. Morgan, J. MacMahan, and A. J. H. M. Reniers, Surf zone physical and morphological regime as determinants of temporal and spatial variation in larval recruitment, *Journal of Experimental Marine Biology and Ecology*, *392*(1), 140–150, doi:10.1016/j.jembe.2010.04.018, 2010.

Simons, R. R., T. J. Grass, and M. Mansour-Tehrani, Bottom shear stresses in the boundary

layers under waves and currents crossing at right angles, *Coastal Engineering Proceedings*, *1*(23), doi:10.9753/icce.v23.%p, 1992.

Smit, P., M. Zijlema, and G. Stelling, Depth-induced wave breaking in a non-hydrostatic, near-shore wave model, *Coastal Engineering*, *76*, 1–16, doi:10.1016/j.coastaleng.2013.01. 008, 2013.

Smit, P., T. Janssen, L. Holthuijsen, and J. Smith, Non-hydrostatic modeling of surf zone wave dynamics, *Coastal Engineering*, *83*, 36–48, doi:10.1016/j.coastaleng.2013.09.005, 2014.

Smith, J. M., S. Bak, T. Hesser, M. A. Bryant, and C. Massey, Frf wave test bed and bathymetry inversion, *Coastal Engineering Proceedings*, *1*(35), 22, doi:10.9753/icce.v35. waves.22, 2017.

Spydell, M., and F. Feddersen, Lagrangian Drifter Dispersion in the Surf Zone: Directionally Spread, Normally Incident Waves, *Journal of Physical Oceanography*, *39*(4), 809–830, doi: 10.1175/2008JPO3892.1, 2009.

Spydell, M. S., The suppression of surfzone cross-shore mixing by alongshore currents, *Geophysical Research Letters*, *43*(18), 9781–9790, doi:10.1002/2016GL070626, 2016.

Stive, M. J. F., and H. G. Wind, A study of radiation stress and set-up in the nearshore region, *Coastal Engineering*, *6*(1), 1–25, doi:10.1016/0378-3839(82)90012-6, 1982.

Stoner, N., and M. Dorfman, Testing the waters: a guide to water quality at vacation beaches, *Natural Resources Defense Council*, *8*(2010), 12, 2007.

Suanda, S. H., and F. Feddersen, A self-similar scaling for cross-shelf exchange driven by transient rip currents, *Geophysical Research Letters*, *42*(13), 5427–5434, doi:10.1002/ 2015GL063944, 2015.

Thornton, E. B., and C. S. Kim, Longshore current and wave height modulation at tidal frequency inside the surf zone, *Journal of Geophysical Research: Oceans*, *98*(C9), 16,509–16,519, doi:10.1029/93JC01440, 1993.

Tissier, M., P. Bonneton, F. Marche, F. Chazel, and D. Lannes, A new approach to handle wave breaking in fully non-linear Boussinesq models, *Coastal Engineering*, *67*, 54–66, doi:10.1016/j.coastaleng.2012.04.004, 2012.

Tonelli, M., and M. Petti, Finite volume scheme for the solution of 2d extended Boussinesq equations in the surf zone, *Ocean Engineering*, *37*(7), 567–582, doi:10.1016/j.oceaneng.2010.02.004, 2010.

Uchiyama, Y., J. C. McWilliams, and A. F. Shchepetkin, Wavecurrent interaction in an oceanic circulation model with a vortex-force formalism: Application to the surf zone, *Ocean Modelling*, *34*(1), 16–35, doi:10.1016/j.ocemod.2010.04.002, 2010.

Uchiyama, Y., J. C. McWilliams, and C. Akan, Three-dimensional transient rip currents: Bathymetric excitation of low-frequency intrinsic variability: 3-D TRANSIENT RIP CURRENTS, *Journal of Geophysical Research: Oceans*, *122*(7), 5826–5849, doi:10.1002/2017JC013005, 2017.

Visser, P. J., Wave basin experiments on bottom friction due to current and waves, *Coastal Engineering Proceedings*, *1*(20), doi:10.9753/icce.v20.%p, 1986.

Warner, J. C., B. Armstrong, R. He, and J. B. Zambon, Development of a Coupled OceanAtmosphereWaveSediment Transport (COAWST) Modeling System, *Ocean Modelling*, *35*(3), 230–244, doi:10.1016/j.ocemod.2010.07.010, 2010.

Zhao, Q., I. A. Svendsen, and K. Haas, Three-dimensional effects in shear waves, *Journal of Geophysical Research: Oceans*, *108*(C8), doi:10.1029/2002JC001306, 2003.

Zijlema, M., and G. S. Stelling, Further experiences with computing non-hydrostatic free-surface flows involving water waves, *International Journal for Numerical Methods in Fluids*, *48*(2), 169–197, doi:10.1002/fld.821, 2005.

Zijlema, M., G. Stelling, and P. Smit, SWASH: An operational public domain code for simulating wave fields and rapidly varied flows in coastal waters, *Coastal Engineering*, *58*(10), 992–1012, doi:10.1016/j.coastaleng.2011.05.015, 2011.